Politecnico di Milano
Scuola di Ingegneria Industriale e dell'Informazione
Corso di Laurea Magistrale in Ingegneria delle Telecomunicazioni
Dipartimento di Elettronica, Informazione e Bioingegneria

Monitoring the Urban Environment with Multitemporal SAR Data

Relatore:
Chiar.mo Prof. Claudio PRATI

Correlatore:
Dott. Ing. Alessandro FERRETTI

Tesi di laurea di:
Gaia ROSSETTI
Matr. 771093

Anno Accademico 2013–2014

To my Family,

Mamma,
Papà,
Federica.
And Pippo, the furry adoptive child.

Acknowledgments

I would like to thank Professor Claudio Prati for introducing me to such an interesting topic that ranged from SAR basics to new applications and for giving me the opportunity of working on real-data, surrounded by experts at *Tele-Rilevamento Europa*. This has been a great experience both from an academic and a professional point of view, allowing me to see how mathematical tools are implemented in the every-day life of an advanced remote sensing company.

I would also like to thank Dr. Alessandro Ferretti and all of the colleagues at *Tele-Rilevamento Europa* for welcoming me in their company. Particularly, I need to thank Dr. Alessio Riucci and Eng. Alfio Fumagalli for helping every time I had a doubt with the development of my thesis.

Finally, two big thank you need to go to two dear friends of mine: to Anna-Cristina Bechmann for all her help with LaTeX and to Sarika Joshi for the 24/7 English-related advice.

But, being this thesis the conclusive chapter of my University years, I cannot but think back at all the people I met, all the experiences I made, all the places I learned to call home. All things that, in a way, contributed to this final result.

To spend an appropriate amount of words for every-thing and every-one that meant something to me throughout this time and to extend my gratitude to all that I wish to specifically thank, is impossible. So here's a list: brief but from the heart.

Milano. Brera. The sunset in Parco Sempione while Ludovico Einaudi is playing the piano. "Il Poli".
Ive and Viz. And whoever knows what a "Cravatta Day" is.
Michele-Luca-e-Ettore.
I Chiacchieroni. Fabrizio, Lucio: I don't have the faintest idea how I'll be able to get through lectures without you two. But then again, I guess there won't be lectures any more.

Telit. The view of maritime pine from my office window.
Claudio Deltin and all of the HR group. It has been such an amazing, interesting summer!

UNITECH. A man playing Catalan songs with his guitar in a sunny late afternoon in Parc Guell. The gala dinner at Castello Sforzesco.

The German Herr that made my final interview, Rana Yavari, Francesca Fogal. The 2012 group.
Best experience I could ever wish for.

Loughborough. Butler Court.
The full moon nights with A-C and Marrria.
Past and future, as it seems.

Mainz. Ooooh Mainz. The Kirschgarten. Mombach. SCHOTT.
Sarika and Christina. I wish I were able to describe how it is possible to become such good friends in a split second. I guess we just knew (and sealed the deal with Vederweisser, halloweening and some good old Weinachtsmarkt)!
The lady that gave me flowers when she had to close her shop. My plants, which I'm trying to raise.

To all of you, THANK YOU.

Abstract

The launch of the TerraSAR-X satellite marked the beginning of the availability of radar systems with spatial resolutions up to one meter and a revisit time of 11 days. These two fundamental features have allowed, in the last six-seven years, the growth of new perspectives in the monitoring of urban environments. Traditional classification algorithms based on image segmentation can now be surpassed by the exploitation of the frequent multi-temporal SAR images, which lead to a pixel-by-pixel analysis. Such improvement could be exploited in order to integrate ISPRA's land use monitoring techniques that, up until now, have been mainly based on optical data, ground monitoring nets and inventories.

This thesis therefore focuses on the implementation of a classification and change detection algorithm characterized by three classes of targets (buildings, vegetation, roads and squares) aimed at urban monitoring applications.

In order to classify the pixels, some mathematical tools such as mean, kurtosis, entropy and the correlation to a seasonal sinusoidal trend have been implemented on the time series of the pixel's amplitude. Buildings time series are characterized by high amplitudes and relatively low entropy; roads and squares time series by low amplitudes, high entropy and high kurtosis; vegetation time series by low amplitudes, high entropy and high correlation to the seasonal trends subjected to a positive phase-shift. Additionally, the estimation of the interferometric coherence of the phase allowed a first rough distinction between the metropolitan area and the surrounding countryside.

During a later stage, the classification algorithm was integrated with a Bayesian change detector. Thanks to this further analysis, it became feasible to classify the targets before and after the change occurred, monitor the growth of new buildings and identify known events.

Finally, two peculiarities that appeared during the development of the thesis became object of investigation. The first one is the presence of buildings that scatter with a sinusoidal trend in time whereas the second one regards the stealth nature of some skyscrapers.

Sommario

Il lancio del satellite tedesco TerraSAR-X ha segnato l'inizio della disponibilità di sistemi radar aventi tempo di rivisitazione di undici giorni ed in grado di produrre immagini caratterizzate da risoluzioni spaziali di un metro. Queste due fondamentali caratteristiche hanno permesso, negli ultimi sei-sette anni, la nascita di nuove prospettive per il monitoraggio urbano. I tradizionali algoritmi di classificazione, basati sulla segmentazione della singola immagine, possono adesso essere superati grazie all'utilizzo delle frequenti immagini SAR che hanno portato ad una analisi pixel-per-pixel. Tale miglioria può essere utilizzata per integrare le tecniche di monitoraggio dell'ISPRA che, ad oggi, sono principalmente basate su dati ottici, reti di monitoraggio a terra ed inventari.

Lo scopo di questa tesi è quindi quello di implementare un algoritmo di classificazione e *change detection* indirizzato ad applicazioni di monitoraggio urbano.

Per poter classificare i pixel sono state effettuate delle analisi statistiche quali media, kurtosi ed entropia ed è stata stimata la correlazione tra la serie temporale dell'ampiezza del pixel ed un andamento stagionale sinusoidale. È stato rilevato come le serie temporali di pixel di edifici siano caratterizzate da ampiezze alte ed entropia relativamente bassa; quelle relative ai pixel di strade e piazze da ampiezze basse, entropia e kurtosi alte; quelle relative ai pixel di vegetazione da ampiezze basse, entropia alta e correlazione con andamento sinusoidale avente sfasamento positivo alta. Inoltre la stima della coerenza interferometrica ha permesso una prima, grossolana distinzione tra area metropolitana e campagna circostante.

Durante una fase successiva, l'algoritmo di classificazione è stato integrato con uno *step detector* baiesiano. Questa ulteriore analisi ha reso possibile la classificazione dei target prima e dopo lo step, il monitoraggio della crescita di nuovi edifici e l'identificazione di eventi noti.

Infine, due caratteristiche che hanno attirato l'attenzione durante lo sviluppo della tesi sono state oggetto di ulteriori analisi: la prima è il fatto che alcuni edifici scatterano in modo sinusoidale nel tempo; la seconda riguarda la natura stealth di alcuni grattacieli.

Contents

List of Figures

List of Tables

Chapter 1

Introduction

Remote sensing from space has been available for civilian applications since the launch of NASA's Seasat in 1978. The former imaging system allowed a 25m $\times$ 25m ground resolution cell and was operational for three productive months. Despite the success of the mission, it was not until 1991 that the European Space Agency launched ERS-1, followed by Canada's RADARSAT in 1995 and by ESA's ENVISAT in 2002. All of the latter systems were characterized by a resolution in the order of tenths of meters and a revisit time that allowed averagely an image per month. It was therefore not until 2007 and the launch of Germany's TerraSAR-X that frequent (one every eleven days) images with resolutions up to 1.5m $\times$ 1m were available for research and commercial applications.

This significant improvement in spatial and temporal resolution provided new possibilities for detailed analysis of urban areas: traditional algorithms, based on image segmentation, can be surpassed by the exploitation of the multi-temporal SAR images that lead to a pixel-by-pixel classification.

Applications are various and range from urban and regional economic development, to census data for undeveloped countries, to the detection of infringement of local building regulations.

Another present application, that has been strongly supported by European environmental programmes and, more specifically, by ISPRA -the Italian Institute for Environmental Protection and Research-, is the monitoring of land use. The increasing demand for living space per person and the increased mobility and growth of transport infrastructure, led to urban sprawl and consequent soli sealing. This important issue has been addressed by various public institutions and land use planning and monitoring is now subjected to European policies and regulations.
The aim of this thesis is therefore to propose a new pixel classification analysis that could integrate ISPRA's monitoring techniques based on the exploitation of the newly available high resolution image time-series.

1.1 The land use problem

Land is a finite resource and it is subjected to competing demands from urbanization, infrastructure, agriculture and the necessity of maintaining vital ecosystem cycles. As a consequence, it needs to be monitored and regulated.

Governmental authorities as the European Commission or, on a local scale, the Italian ISPRA, are therefore undertaking environmental projects aimed at a strategic land use and protection.

In 2006 the European Commission defined soil as an extremely complex living medium that is formed by mineral particles, organic matter, water, air, and living organisms.

Soil is responsible for many vital environmental, economic, social, and cultural functions that include the production of food as well as filtration and transformation of water, carbon, and nitrogen.

Soil degradation, caused by sealing, contamination, erosion, loss of organic matter, salinization, desertification and other threats, has serious and long-term consequences for human health, natural ecosystems, and the economy.

The two main consequences of unregulated land use are urban sprawl and soil sealing. Urban sprawl is an unplanned urban development, characterized by a low density mix of land uses on the urban fringe. Formerly identified as a US-localized phenomenon associated with the low-density outward expansion of US cities, it has more recently been developing around European cities as well. This expansion of urban areas led to a marked acceleration in soil sealing, which is the main cause of land degradation. In fact, the land water-proofing that results from the use of cement and other construction materials, may cause serious issues such as increased flood probability, the so called *heat islands* and an inhibition of the natural biological cycles.

In 2011 the European Commission set as a 2050 goal a 0% increment in land use. In order to achieve this ambitious purpose politics have been oriented towards the limitation, mitigation and compensation of soil sealing. Additionally, monitoring sources have been established.

At European level, land use monitoring systems are:

- CORINE Land Cover (satellite optical images);
- Copernicus (both satellite and in-situ data. The system provides optical, radar, altimetric, meteorological, radiometric and spectrometer information);
- LUCAS (survey originated statistics).

Additionally, at Italian level:

- ISPRA's land use monitoring net;

- Refresh (aerial photos);
- POPOLUS (the *Permanent Observed Points for Land Use* inventory);
- IUTI (the textitInventario dell'Uso delle Terre in Italia inventory);
- ISTAT (statistical data);
- Data from the *Regioni* (the regional authorities).

Despite this apparently vast amount of data, relevant, detailed information is not available with a uniform coverage and not all of the databases use the same reference units. Furthermore, classification errors are estimated at around 15% [1].

For all of the above considerations, it is of primary importance to integrate the present monitoring net with a high-resolution, homogeneous data-acquiring system and a reliable, automatic classification algorithm.

1.2 Outline

The current chapter is of an introductory nature. The main objectives addressed by this thesis and the tools and work methodologies are presented and the applications listed.

In the second chapter, the grounds for understanding radars and the concepts behind SAR imaging are illustrated. Initially, a comparison between optical and radar images is outlined, followed by a description of the general principles of Synthetic Aperture Radar and TerraSAR-X; the specific platform used to acquire the images that were analyzed within the scope of this thesis. Subsequently, all the required practical knowledge of targets and reflectivity are presented. Finally, a brief introduction to interferometry is provided.

In the third chapter, the theoretical background needed for time series analysis aimed at classification is illustrated. In the first section the instruments needed for the identification of the statistical properties of the time series are described. In the second section a brief outline on the correlation with known meteorological events is provided. In the last section, single and multiple step detectors are discussed.

In the fourth chapter, the results achieved with the classification and change detection algorithms are illustrated. Firstly, an introduction of the area under investigation and related data-set is provided, followed by the description of time series analysis implementation. In the third, main section three types of classification are described: one obtained with interferometric coherence, one with the standard classification algorithm proposed in this thesis and finally one resulting from change detection results. In the conclusive paragraph two peculiarities that had been observed during the implementation of the work, are discussed.

Chapter 2

Basics on radars and SAR imaging

In the following chapter, the basis for understanding radars and the concepts behind SAR imaging will be presented.

Initially, a comparison between optical and radar images will be outlined in order for the specificities of the two systems to be fully appreciated and the advantages that distinguish SAR images identified.

Secondly, the general principles of Synthetic Aperture Radar will be discussed, followed by a description of TerraSAR-X; the specific platform used to acquire the images that were analyzed within the scope of this thesis.

Subsequently, since any interpretation of radar imagery requires a thorough understanding of the phenomenology of the interactions between electromagnetic waves and the texture and composition of the environment, all the required practical knowledge of targets and reflectivity will be presented.

Finally, a brief introduction in interferometry will be provided.

2.1 Comparison between optical and radar images

Optical and radar images differ for a series of factors that originate in the very nature of their systems.

1. Optical systems operate in the visible wavelength range: 380nm $\leq \lambda_{optical} \leq$ 760nm. As a result, optical sensors cannot see through clouds and fog. Radar sensors, on the other hand, operate in the microwave domain and have wavelengths in the order of centimeters. In the X-band 2.5cm $\leq \lambda_{Xband} \leq$ 3.75cm. Due to the fact that the wavelength is much longer than the single drop of water or fog particle, radar systems are able to create images under any weather condition;

2. Optical systems are passive devices whereas radar systems are active ones: radar images are created by illuminating the area of interest with electromagnetic pulses. For this reason they are completely independent from sun

illumination and are able to generate images both during the day and the night [2];

3. Radars are coherent sensors and can therefore record both amplitude and phase information for every target (as opposed to optical images that acquire only amplitude data). Resulting from this additional information, sensor-target distances can be computed very precisely;

4. SAR is a side-looking sensor whereas optical systems are also able to look straight down towards nadir.

Due to all of the above features, the selection of radar rather than optical systems strongly depends on the application. For instance, radars are to be preferred from their optical counterparts in the event that their reliability in providing images at a specific point in time is required.

2.2 Synthetic aperature radar

The term radar finds its roots in the acronym of the English expression *Radio Detection And Ranging*. These systems work by exploiting the information contained in electromagnetic waves that propagate and reflect in a targeted environment. Radars can be used to evaluate distances, detect and track moving targets and create images.

Synthetic Aperture Radar is a side-looking microwave radar whose main purpose is to make high-resolution, coherent images of the Earth. They were developed as a means of overcoming the limitations of real aperture radars by using the orbital path of the satellite as a virtual antennae array and consequently combining the various low-resolution images made by its sensor along the flight path into one high-resolution image.

The use of microwaves enables the SAR to penetrate clouds and be independent from sun illumination, sensible to surface roughness, penetrate through foliage and canopy (in case of sufficiently long wavelengths) and allow accurate localization.

2.2.1 SAR acquisition geometry and operational modes

The geometry of a typical spaceborne SAR is as is depicted in Figure 2.1: the satellite, moving along its orbital path, carries a SAR sensor which points perpendicularly to the flight direction and down towards Earth with a specific look angle that defines the slant range direction. The angle between the slant range and the zenith is the *incidence angle*. The projection of the orbit on Earth is called the *ground track* and the area imaged by the radar beam is called radar *swath* [3].

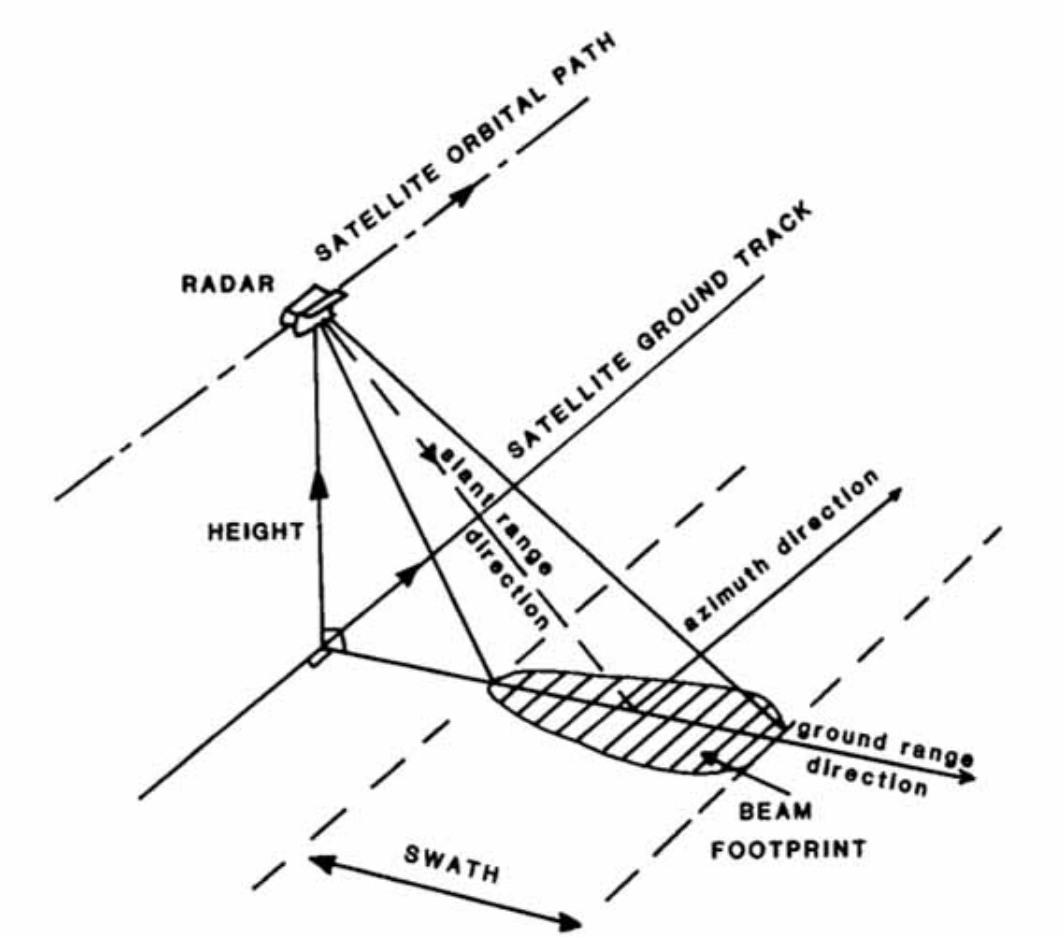

Figure 2.1: Geometry of a spaceborne SAR

In the SAR image, the direction of the satellite's movement corresponds to the azimuth direction, while the imaging direction corresponds to the range direction.

All modern SAR satellites orbit the Earth on a near-polar orbit. Given the fact that by default they are right-looking sensors, their look direction is either east or west according on whether they have an ascending or descending orbit. This fact is depicted in Figure 2.2.

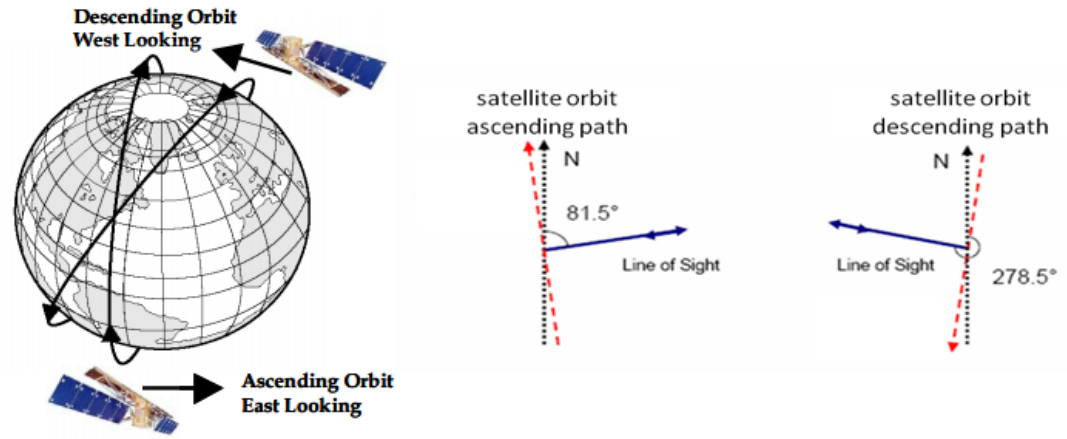

Figure 2.2: Ascending and descending orbits

The basic SAR acquisition geometry can be modified in order to acquire better resolutions or an increased observation area. These system's variations are called operational modes and fall under four main categories:

- *Stripmap*: this is the standard operational mode to which the geometry depicted in Figure 2.1 corresponds to;
- *Spotlight*: this is an operational mode characterized by increased azimuth resolution. In order to achieve this while still maintaining the same system's specifications, the target needs to be followed by the antenna for a longer time with respect to the standard mode. This can be done at the cost of a reduction of the area under investigation;
- *Scansar*: this is an operational mode characterized by increased swath width (e.g. higher coverage along the range direction). Such an advantage can be achieved by processing several sub-swaths with simultaneous beams, each with a different incidence angle. This can be implemented at the cost of reduced azimuth resolution;
- *Tops*: this is a more efficient and flexible wide-swath mode. It constitutes an alternative to *scansar*.

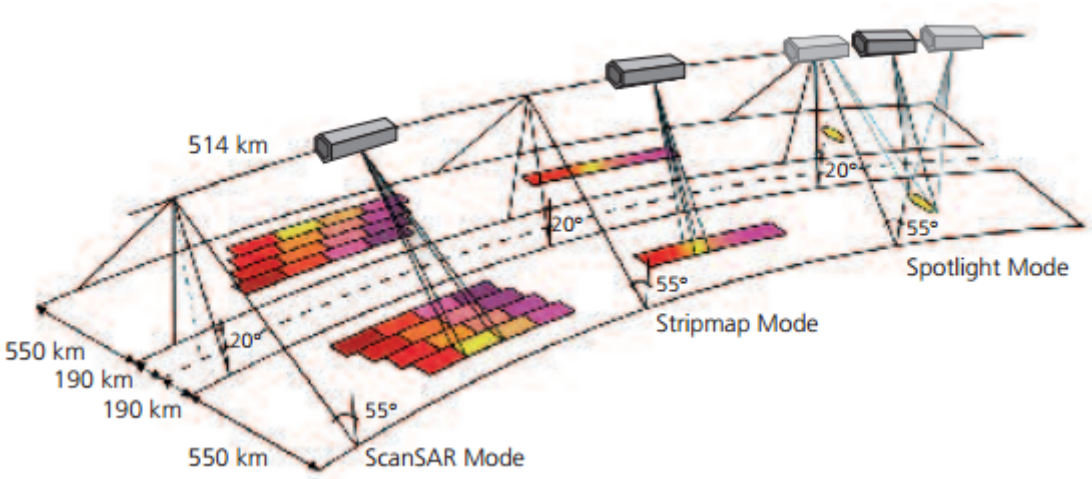

Figure 2.3: SAR operational modes. The mentioned parameters are specific to the TerraSAR-X platform

2.2.2 SAR resolution

The resolution of the radar depends both on the system's bandwidth and on the acquisition geometry.

The *range resolution* depends on the system's bandwidth and it can be calculated with Formula 2.1:

$$\rho_r = \frac{c}{2B} \tag{2.1}$$

Whereas, as it can be seen in Formula 2.2, the ground cell is characterized by a range resolution that also depends on the look angle and the terrain slope:

$$\rho_{r,groundrange} = \frac{\rho_r}{\sin(\theta_{Incidences})} = \frac{c}{2B\sin(\theta - \alpha)} \tag{2.2}$$

In a SAR system, the *azimuth resolution* depends on its synthetic aperture, e.g. on the coherent summation of the echoes obtained by the radar along its synthetic length. It can be calculated as:

$$\rho_{az} = \frac{\lambda}{2L_s} r_0 \tag{2.3}$$

Where L_s is the length of the synthetic aperture and r_0 is the distance between the satellite and the target along the range direction [4].

2.2.3 The radar equation

The radar equation quantifies the process that connects the transmitted wave, the free space propagation, the incidence with the target and the received wave.

The scattering geometry is depicted Figure 2.4:

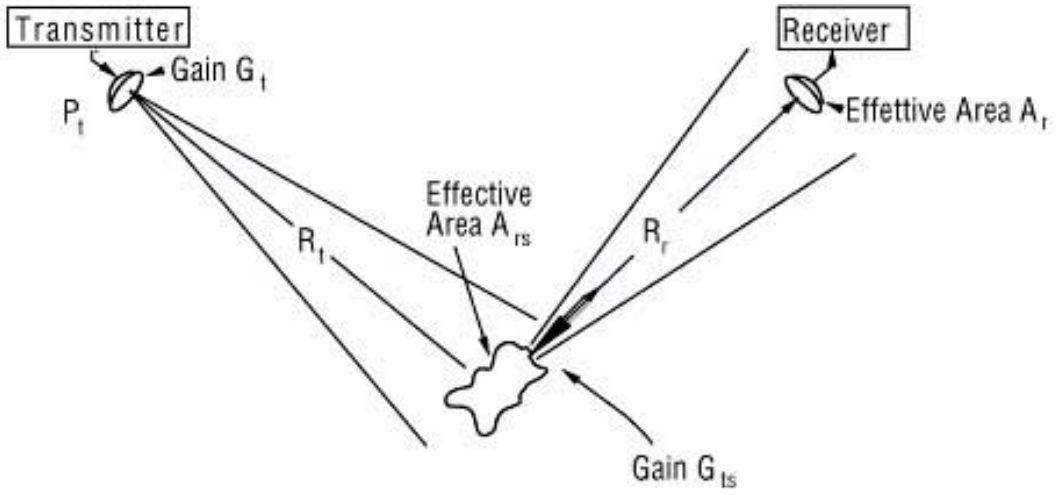

Figure 2.4: Radar equation geometry

A transmitter characterized by transmission gain G_t, sends a signal with transmission power P_t towards a target at distance R_t. The target, whose properties can be summarized by the Radar Cross Section (the RCS amplitude has the dimensions of a surface), reflects the signal towards a receiver at distance R_r that is characterized by and effective area $A_{eff,r}$.

The received power can be therefore calculated with Formula 2.4:

$$P_r = \frac{P_t G_t}{4\pi R_t^2} \times \sigma \times \frac{A_{eff,r}}{4\pi R_r^2} \tag{2.4}$$

Where:

- P_t and P_r are the transmitted and received power;
- G_t is the transmitted antenna gain. The antenna gain relates the intensity of an antenna in a given direction to the intensity that would be produced by a lossless, isotropic antenna;
- $4\pi R^2$ is the free space attenuation. For the SAR case, $R_t \cong R_r$;
- σ is the Radar Cross Section, which is a parameter that characterizes the target (for additional information refer to section 2.4.2);
- A_{eff} is the effective area of the antenna, a parameter which is proportional to the gain: $A_{eff} = G\frac{\lambda^2}{4\pi}$.

Taking thus into account the abovementioned considerations, the radar equation can be re-written as:

$$P_r = \frac{P_t G_t G_r \lambda^2}{(4\pi)^3 R^4} \sigma \tag{2.5}$$

The received power is therefore defined by three main features:

1. The characteristics of the system (transmitted power, antenna features and wavelength);
2. Distance between satellite and target;
3. Target properties.

2.3 TerraSAR-X and other SAR systems

The history of spaceborne Synthetic Aperture Radars began on the 27th of June 1978 with the launch of NASA's Seasat with the aim of demonstrating the feasibility of orbital remote sensing for ocean observation applications. Although Seasat suffered a power failure that caused the end of the mission, just three months later, the satellite had already collected more synthetic aperture radar information regarding the surface of the ocean than had been acquired in the previous 100 years of shipboard research [5].

Seasat was characterized by the following system's specifications:

Seasat Specifications (NASA, 1978)	
Radar Frequency	1.275GHz (L-band)
Wavelength	23.5cm
Resolution	25m × 25m
Revisit	17 days
Incidence Angle	23°
Polarization	HH

Table 2.1: Seatsat specifications

Thirteen years later, in 1991, the European Space Agency launched the ERS-1 satellite. From this point onwards, SAR sensors began acquiring data in a constant manner. ERS-1 and the most important satellites that followed were, and in some cases still are, characterized by the specifications listed in the following tables.

ERS-1 Specifications (European Space Agency, 1991)	
Radar Frequency	5.3GHz (C-band)
Wavelength	5.6cm
Resolution	30m
Revisit	35 days
Incidence Angle	23°
Polarization	VV

Table 2.2: ERS-1 specifications

RADARSAT-I Specifications (Canadian Space Agency, 1995)	
Radar Frequency	5.3GHz (C-band)
Wavelength	5.6cm
Resolution	8m fine, 30m standard, $50-100$m scanSAR
Revisit	24 days
Incidence Angle	34° - 47°fine, 20° - 49°standard and scanSAR
Polarization	HH

Table 2.3: RADARSAT-1 specifications

ERS-2 Specifications (European Space Agency, 1995)	
Radar Frequency	5.3GHz (C-band)
Wavelength	5.6cm
Resolution	30m
Revisit	35 days
Incidence Angle	23°
Polarization	VV

Table 2.4: ERS-2 specifictations

ENVISAT's ASAR Specifications (European Space Agency, 2002)	
Radar Frequency	C-band
Wavelength	$4-5$cm
Resolution	30m stripmap, $150-1000$m scanSAR
Revisit	35 days
Incidence Angle	15° - 45°
Polarization	VV, HH, HV, VH

Table 2.5: ENVISAT's ASAR specifictations

RADARSAT-II Specifications (European Space Agency, 2007)	
Radar Frequency	5.4GHz (C-band)
Wavelength	5.5cm
Resolution	3m spotlight, 10m fine, 25m standard, 300m scan
Revisit	24 days
Incidence Angle	20° - 49°
Polarization	HH, VV, VH, HV

Table 2.6: RADARSAT-II Specifications

Cosmo-SkyMed Specifications (European Space Agency, 2007)	
Radar Frequency	X-band
Wavelength	3.1cm
Resolution	1m spotlight, $3-5$m stripmap, $30-100$m scan
Revisit	16days
Incidence Angle	25° - 50°
Polarization	HH, VV, HV, VH

Table 2.7: Cosmo-SkyMed Specifications

SENTINEL-1A Specifications (European Space Agency, 2014)	
Radar Frequency	5.405GHz (C-band)
Wavelength	5.5cm
Resolution	5m × 5m in Strip Map mode
Revisit	12days
Incidence Angle	20° - 47°
Polarization	HH+HV, VV+VH

Table 2.8: SENTINEL-1A Specifications

Finally, specific emphasis needs to be placed on TerraSAR-X, the German Earth observation satellite whose images have been analyzed is this study. Its mission began on the 15th June 2007, with the aim of providing SAR data in the X-band for research and development purposes as well as scientific and commercial applications.

TerraSAR-X was the first civilian radar system able to provide spatial resolutions up to one meter and a revisit time of eleven days. These two fundamental features allowed, in the last six-seven years, the growth of new perspectives in the monitoring of urban environments.

TerraSAR-X Specifications	
Length	4.88cm
Diameter	2.4m
Radar Frequency	9.65GHz
Wavelength	3.1cm
Resolution	1m (High Resolution SpotLight mode) 3m (StripMap mode) 16m (ScanSAR mode)
Orbital Altitude	514km
Pulse Repetition Frequency	3kHz $-$ 6.5kHz
Revisit	11days
Inclination Angle	97.44°
Incidence Angle	20° - 55°
Polarization	HH, VH, HV, VV

Table 2.9: TerraSAR-X Specifications

2.4 Understanding SAR images

In order to decipher SAR images, it is of primary importance to acquire a thorough understanding of targets, their interaction with electromagnetic waves and the parameters that influence the resulting amplitude at the receiver.

2.4.1 Parameters affecting reflectivity

The factors affecting the final amplitude of the pixels in the SAR image are many and related to complex interactions. The three main factors are radar system parameters, target properties (where a target is a ground object that reflects the electromagnetic wave back to the radar) and environmental variables.

- The frequency of the radar: this parameter determines both the penetration depth of the electromagnetic waves in the target, both the perceived roughness of the surface under investigation. This parameter is of particular interest towards the application discussed in this study as, in case a platform with a longer wavelength were to be considered for future developments, buildings hidden under the canopy could be detected.
- The polarization of the wave emitted by the radar: polarization describes the orientation of the electric field component of the emitted electromagnetic wave and can therefore provide information on contingent layers of the target or on the form and orientation of distributed scatterers. It has been empirically demonstrated that, by modifying the used polarization, specific ground features become more or less visible, according to the system's variation and that HV-polarized images appeared to be the best for detecting urban areas, followed by HH and VH polarized images [6].
- The radar's look direction: the look direction strongly influences the radar signature in relation to the orientation of ground objects. Due to the fact that many cities and towns have features with a northern-southern or easterly-westerly orientation, the effect of look direction on the orientation of urban settlements has been referred to as the *cardinal effect*. Clear examples in the city of Milan are *viale Monza* and the *Naviglio Pavese*: all the dihedral reflectors between the roads and the houses backscatter all the energy towards the radar which faces them perfectly, thus resulting in higher amplitudes with respect to average.

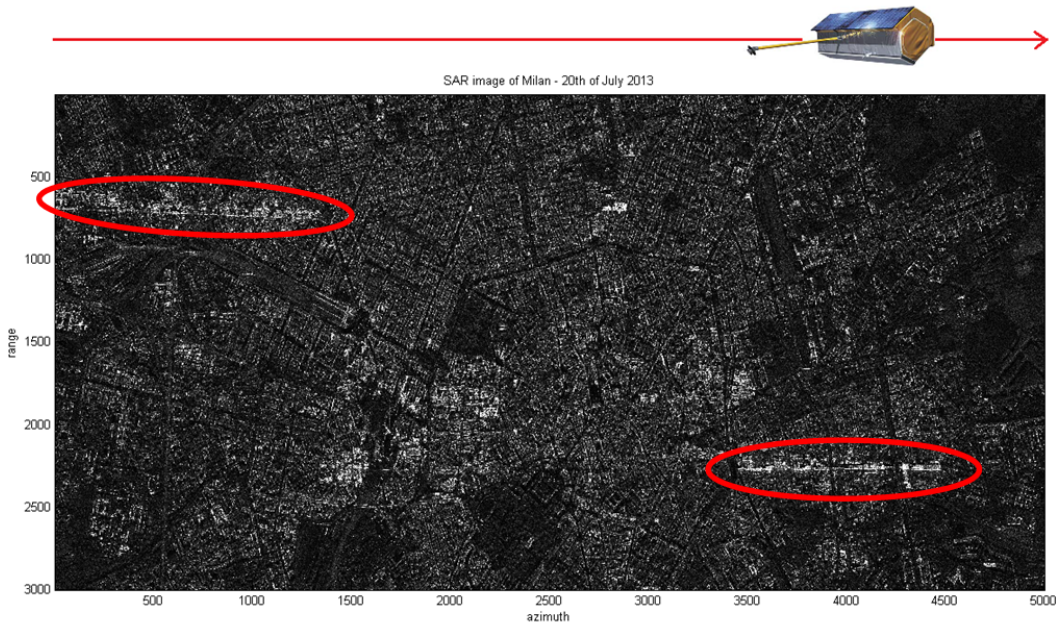

Figure 2.5: SAR image of Milan and representation of the orbital path from which TerraSAR-X acquired the data. Due to their optimal geometry *viale Monza* (on the top-left) and the *Naviglio Pavese* (bottom-Right) can be immediately identified.

- The incidence angle of the electromagnetic wave: incidence (depression) angles have control over the range resolution and affect shadow lengths. In 1990 Henderson concluded that angles of less than 20° were of minimal utility for settlement detection in northern-boreal forest environments;
- The dielectric constant of the target: the electrical properties of a surface, critically affect radar returns as they determine the transmission/reflection coefficients of the electromagnetic waves;
- The geometric characteristics of the target: the geometry of the target determines whether a deterministic or a random scattering occurs and the direction along which it is being forwarded;
- Environmental factors: environmental factors such as humidity in the air and temperature also contribute to the radar's response.

2.4.2 Target parameters affecting reflectivity: dielectric constant and geometry

Provided that the images within the data-set that has been analyzed in this study all originate from the same radar system (e.g. TerraSAR-X), the parameters that cause diversity in the backscatter are the ones related to the targets. These are the dielectric constant and the target's geometry within the resolution cell.

The target's dielectric constant is a key contributor due to the fact that electromagnetic wave reflections are caused by the impact of the signal against a medium characterized by a relative permittivity differing from the one that characterizes air

(the previous medium). The greater the difference (that is maximized for perfect conductors), the bigger the amount of reflected wave.

As for geometry, if there is only one predominant scatterer (such as a parabolic dish), the ground object is called a *point target*. If, on the other hand, there are several independent scatterers (such as the leaves and branches of a tree) the ground object is called a *distributed target*. A perfectly smooth flat surface will reflect all of the signal away from the target resulting in zero amplitude (effect of a lake) whereas a properly oriented parabolic dish will send all of the energy back towards the radar. A distributed target, on the other hand, needs to be modeled as a stochastic random process that leads to constructive and destructive summations. Due to all of the above examples, it appears clear that the geometry of the targets within the resolution cell is another key contributor.

The target's contribution is accounted for in the radar equation by the Radar Cross Section. This is a complex coefficient that defines the scattering behavior of the target. It is defined as a measure of the power that a target scatters in a given direction when illuminated by an incident wave, normalized to the power density of the incident wave at the target. The normalization is necessary in order to remove the effects of the distance radar-target and the effects of the transmitter power level [7].

2.4.2.1 Dielectric constant

In case of an ideal smooth surface, the characteristics of reflection and transmission can be calculated through the Fresnel equations (assuming to work in the far field with respect to the wavelength, it is correct to use geometric optics to compute reflections and refraction).

Under these conditions, the SAR won't receive any signal back as all of the transmitted power will be reflected away from the radar. As it will be seen in section 2.4.2.2, in real case scenarios the roughness of the surface and the presence of multiple bounces will provide backscatter. These interactions, though, are not objective of this section that analyses an over-simplified model in order to clarify the influence of the dielectric component on the received signal.

The Fresnel Equations for perpendicularly polarized light are:

- Reflection coefficient: $r_\perp = \dfrac{n_i \cos\theta_i - n_t \cos\theta_t}{n_i \cos\theta_i + n_t \cos\theta_t}$;
- Transmission coefficient: $t_\perp = \dfrac{2n_i \cos\theta_i}{n_i \cos\theta_i + n_t \cos\theta_t}$.

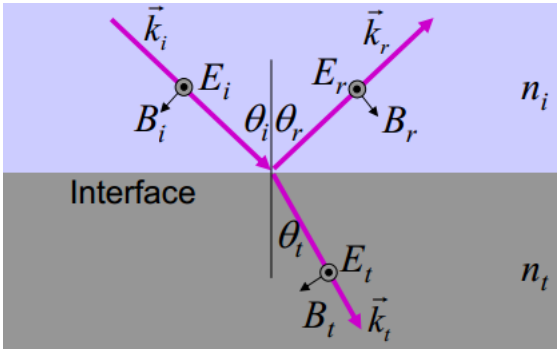

Figure 2.6: Depiction of Fresnel's reflection and transmission interactions for perpendicularly polarized light

The Fresnel Equations for parallel polarized light are:

- Reflection coefficient: $r_{\parallel} = \dfrac{n_i \cos\theta_t - n_t \cos\theta_i}{n_i \cos\theta_t + n_t \cos\theta_i}$;
- Transmission coefficient: $t_{\parallel} = \dfrac{2n_i \cos\theta_i}{n_i \cos\theta_t + n_t \cos\theta_i}$.

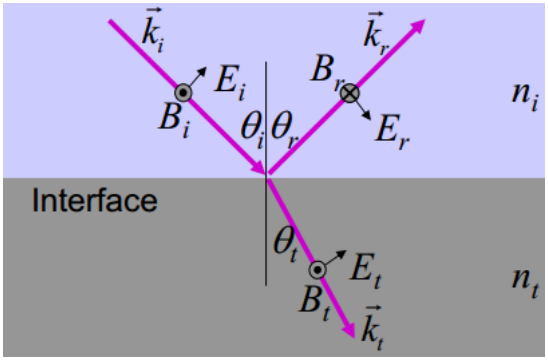

Figure 2.7: Depiction of Fresnel's reflection and transmission interactions for parallel polarized light

For the case under investigation, the upper medium is air, hence $n_i = 1$. Assuming also for simplification normal incidence (e.g. $\theta_i = 0$), the reflection and transmission coefficients are independent to polarization and reduce to Equations 2.6 and 2.7:

$$r = \frac{n_i - n_t}{n_i + n_t} = \frac{1 - n_t}{1 + n_t} \tag{2.6}$$

$$t = \frac{2n_i}{n_i + n_t} = \frac{2}{1 + n_t} \tag{2.7}$$

By means of these formulas it can be easily appreciated that, if the second medium is a perfect conductor ($n_t \to \infty$) there is total reflection ($r \to -1$) and obviously zero transmission ($t \to 0$). The more similar n_t gets to n_i, the stronger will get

the transmitted component with respect to the reflected one (as if there were no interface).

This is the reason why the dielectric constant has such a strong influence on the backscattered signal strength.

2.4.2.2 Geometry

The geometry of the target can be divided into two main sub-categories according to whether the target is deterministic or random (or, in other words, whether it is a point scatterer or a distributed one).

2.4.2.2.1 Geometry of point scatterers

- Reflection from a smooth flat surface: when the surface is perfectly smooth compared to the wavelength of the system, the electromagnetic wave reflects as described by the law of reflection. Being the incidence angle equal to the reflection angle, either all of the energy is backscattered away from the radar (as it happens for wave-less water basins, as shown in Figure 2.9) or, in the event of normal incidence, the total energy returns towards the radar.

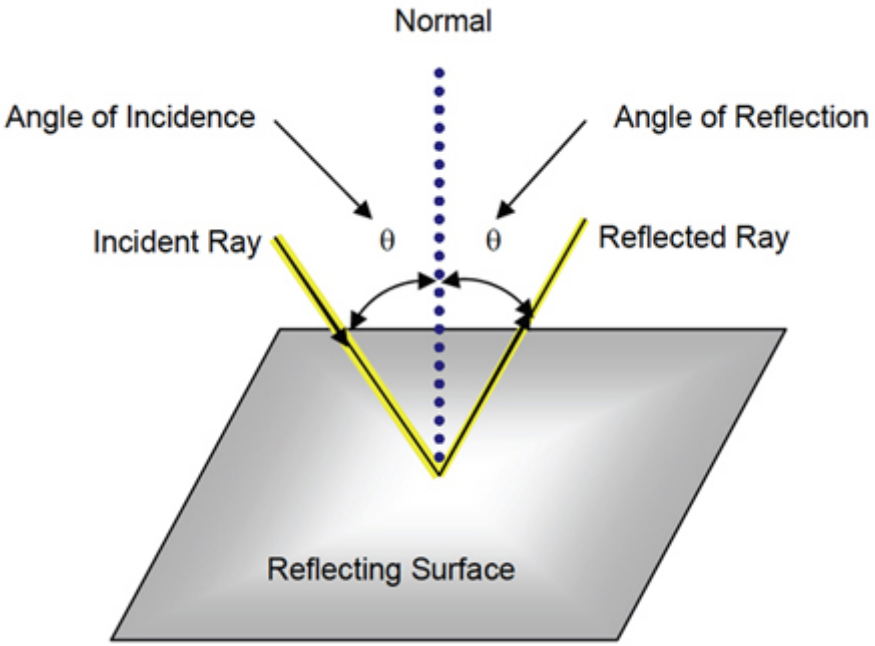

Figure 2.8: Reflection from a smooth flat surface model.

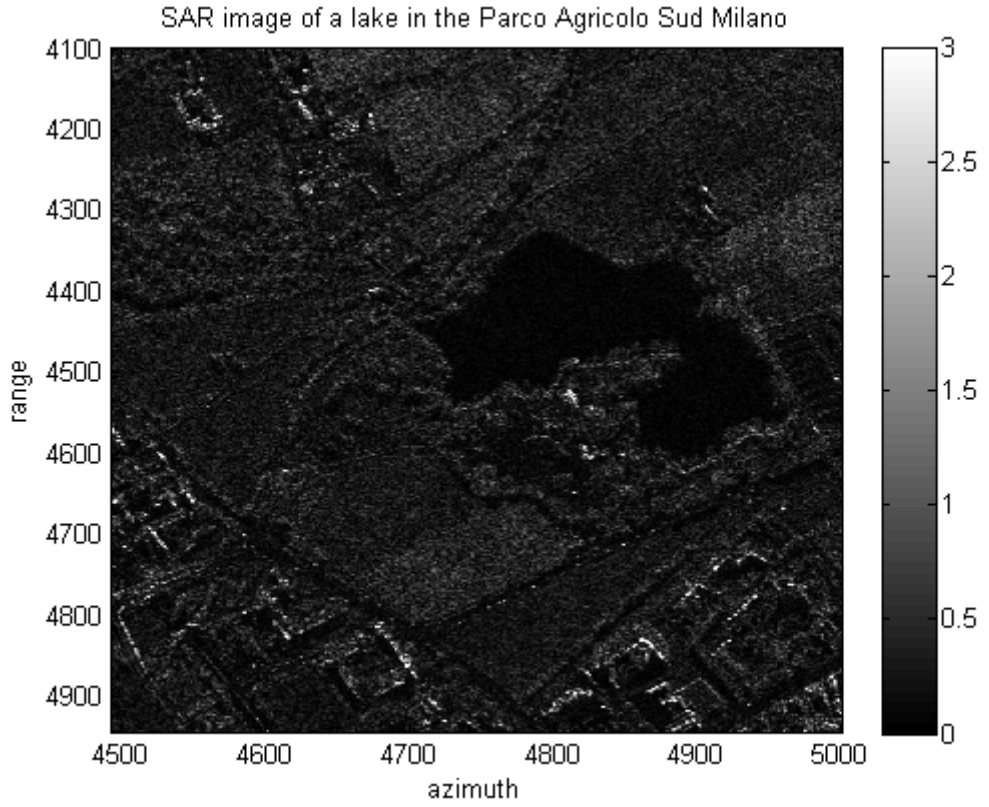

Figure 2.9: SAR image of a lake in the *Parco Agrucolo Sud Milano*. The water basin distinguishes itself because of its zero amplitude.

- Reflection from a Dihedral corner: a dihedral corner (as sketched in Figure 2.10) is the combination of two flat surfaces oriented at 90° from one another. Although perfect dihedral reflectors are rare, this is a very common shape within urban environments (an example is the angle between every pavement and building's facade -although this is not ideal since the two sides are characterized by different dielectric constants and sometimes roughness parameters). As previously mentioned and depicted in Figure 2.5, if the wall of the building is almost parallel to the SAR azimuth direction, this double bounce effect will provide a particularly strong backscatter.

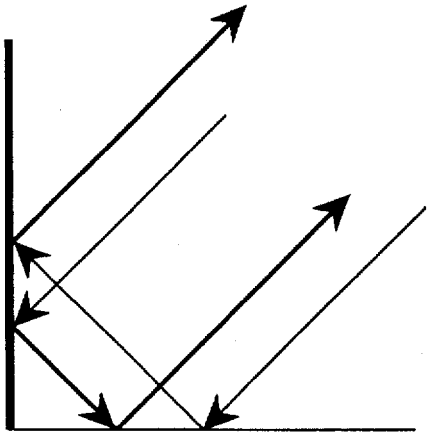

Figure 2.10: Dihedral corner reflector model.

- Reflection from a Trihedral corner: a trihedral corner (as sketched on the left-hand side of Figure 2.11) is the combination of three flat surfaces, all mutually perpendicular. Due to the fact that the reflection is characterized by a triple bounce in a 3D space, trihedral corners provide a very strong backscatter even if not perfectly oriented. As a consequence, artificial trihedral corner reflectors are often used to calibrate SAR images (an example is depicted on the right-hand side of Figure 2.11).

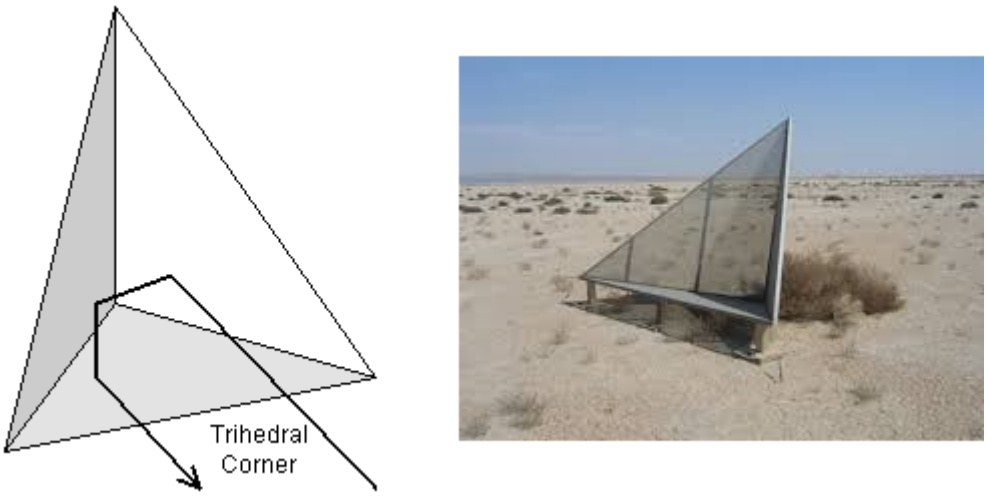

Figure 2.11: Trihedral corner reflector model (on the left) and SAR image calibration devise (on the right).

- Reflection from a Sphere: due to the fact that a sphere reflects the signal isotropically (refer to Figure 2.12), it provides a very low backscatter. It is for this same reason that the *B-2 stealth bomber* has such a round and smooth fuselage.

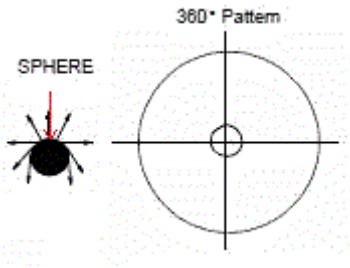

Figure 2.12: Spherical reflector model and radiation pattern.

2.4.2.2.2 Geometry of distributed scatterers

- Scattering from a rough flat surface: when the surface is rough compared to the wavelength of the system, the scattering mechanism is no longer deterministic and the reflectivity function becomes random. Roughness is typically measured as the root mean square height of the micro-relief in the terrain and in order to estimate the minimum roughness height after which the roughness is detected by the radar, the Rayleigh Criterion can be evaluated. As depicted in Figure 2.13, the bigger the roughness, the bigger the diffuse field component becomes with respect to the coherently reflected one.

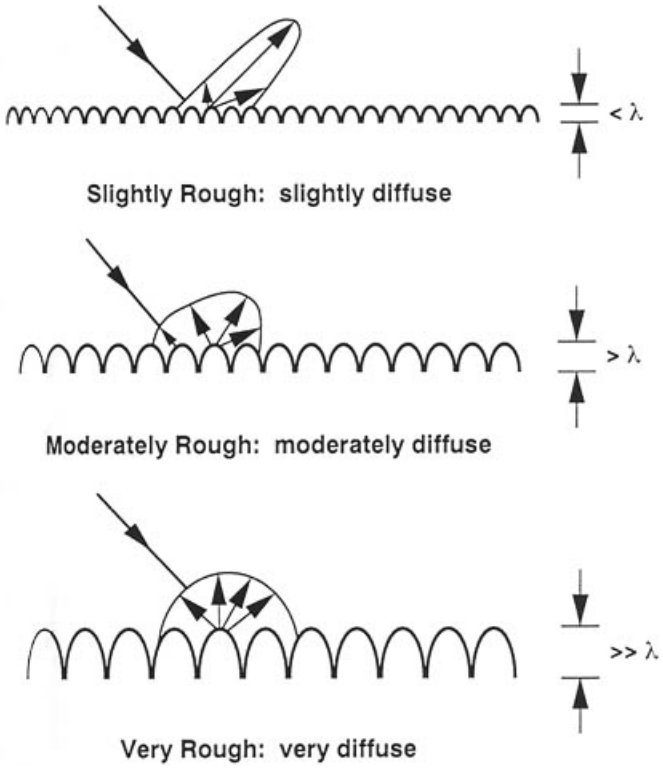

Figure 2.13: Models for rough surfaces. The diffused electromagnetic component increases as the root mean square height of the roughness increases.

- Bragg scattering: when the scatterers are positioned with a regular pattern that repeats itself at distances that are proportional to the projection of the

radar's wavelength on the ground, they will create a strong constructive interference effect that goes under the name of Bragg scattering. This target's characteristic is typical of the wavelets produced by the wind on water surfaces (refer to Figure 2.14).

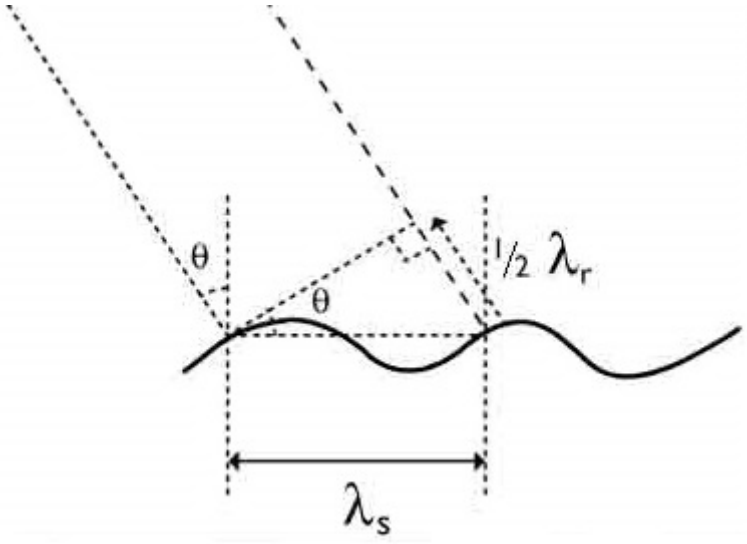

Figure 2.14: Bragg scattering model for sea wavelets.

- Volume scattering: when elementary scatterers are randomly distributed throughout a supporting layer, the radar receives a signal that can be modeled by a stochastic random process. Assuming for simplification a linear behavior of the composite target, the backscattered signal results thus in a superposition of the N returns from the N targets within the resolution cell, each delayed according to their specific travel path. The noise related to the random fluctuations of this constructive/destructive summation is called *speckle*. As depicted in Figure 2.15, this model is particularly accurate for vegetation pixels. Also, in Figure 2.16 a real-data example has been provided: the single SAR image of a green area is strongly affected by speckle noise (on the left-hand side) whereas the average between 126 images in time compensates for the random fluctuations (on the right-hand side).

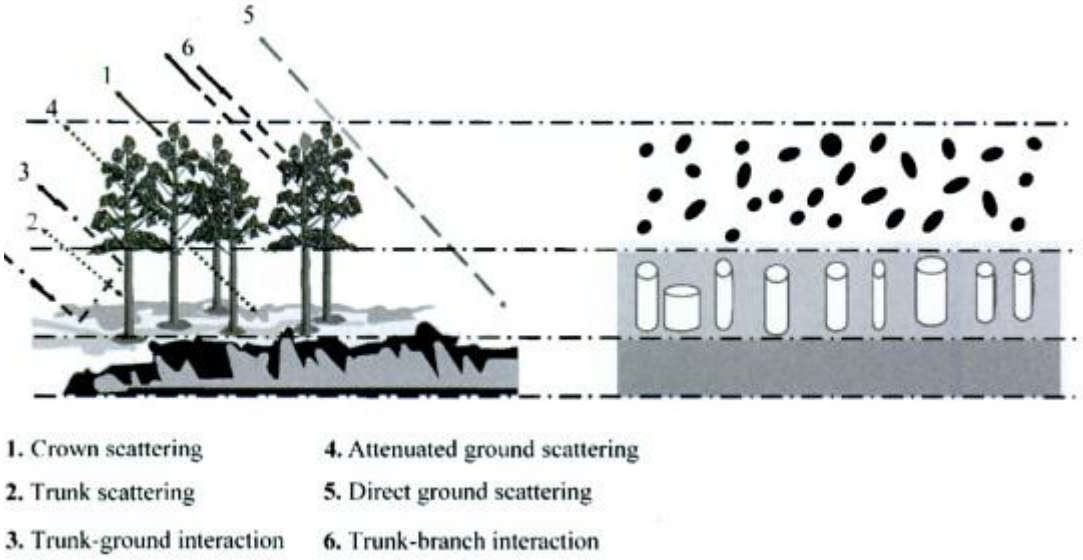

Figure 2.15: Model for vegetation volume scattering.

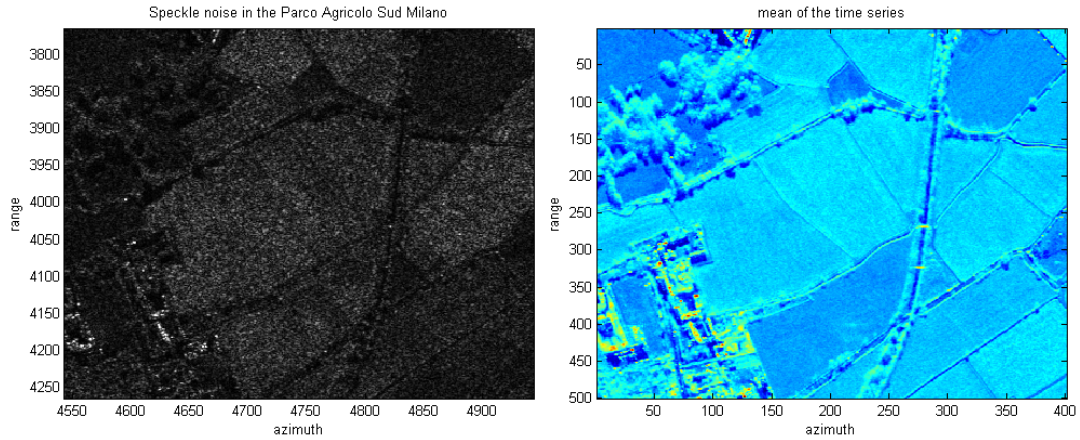

Figure 2.16: Volume scattering example. The single SAR image of a green area it strongly affected by speckle noise (on the left) whereas the average between 126 images in time compensates for the random fluctuations (on the right).

2.4.3 Geometry related deformations: shadowing, layover and foreshortening

The combination of geometry and sampling grid may cause a series of artefacts that distort the image. These effects, that are depicted in Figure 2.17, fall under three main categories:

- *Shadowing* occurs when a target's "back" (e.g. the side that is not directly facing the radar) is steeper than the sensor's depression angle. This causes the presence of a black area (zero signal) behind the aforementioned object;
- *Layover* occurs when a target is so steep that:

- It's base is at the same distance from the radar as its top, therefore causing ambiguity;
- It's base is further away from the radar with respect to the top, therefore causing an inversion in the order of the surface elements;

- *Foreshortening* is conceptually quite similar to layover, as they both originate from the fact that radars work by measuring signal travel time and not angles as optical systems do. It occurs when, being the distance between the target's top and the SAR quite similar to the distance between the target's base and the SAR, the radar does not recognize them as respectively afar. This reflects in the image as the "leaning" of the summit of the body towards the observer [8].

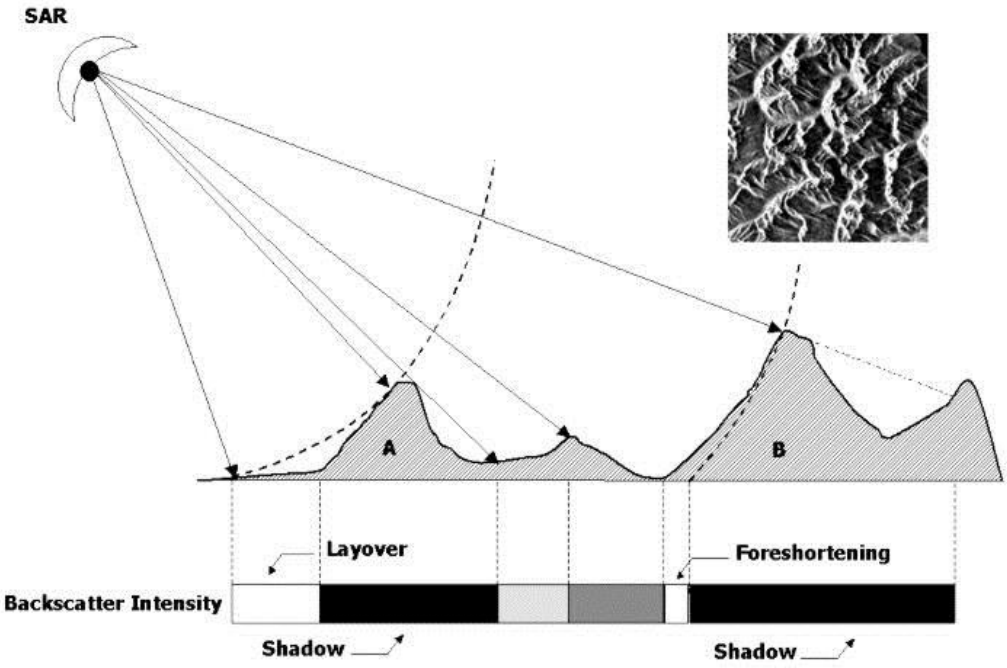

Figure 2.17: Depiction of the different types of radar geometric distortion.

2.5 Interferometry basics

Given the aim of this thesis, minimal attention has been so far allotted to the phase received by the radar along with the amplitude.

The phase of the received signal carries the information of the distance between the radar and target along the range direction.

The techniques that exploit the information contained on the phase go under the name of *Interferometry*.

In the event that two or more acquisitions are provided, two major interferometry applications can be obtained:

- Availability of two acquisitions displaced in space (but acquired at the same time): the target can be localized in the 3D space leading thus to the estimation of a Digital Elevation Model;
- Availability of two acquisitions displaced in time (but ideally acquired from the same place): the line of sight variations can be detected leading thus to the identification of deformations or along-track motions.

The first acquisition is called *master* and the ones that are used as a comparison are called *slave* observations.

The geometry that characterizes interferometric systems is as depicted in Figure 2.18.

The distance between acquiring sensors is called *baseline*.

The *spatial baseline* is a vector in the 3D space that goes from the master satellite to the slave satellite. It can be given in terms of its normal and parallel components (with respect to the range direction).

The *temporal baseline* carries the information of time separation between master and slave acquisitions.

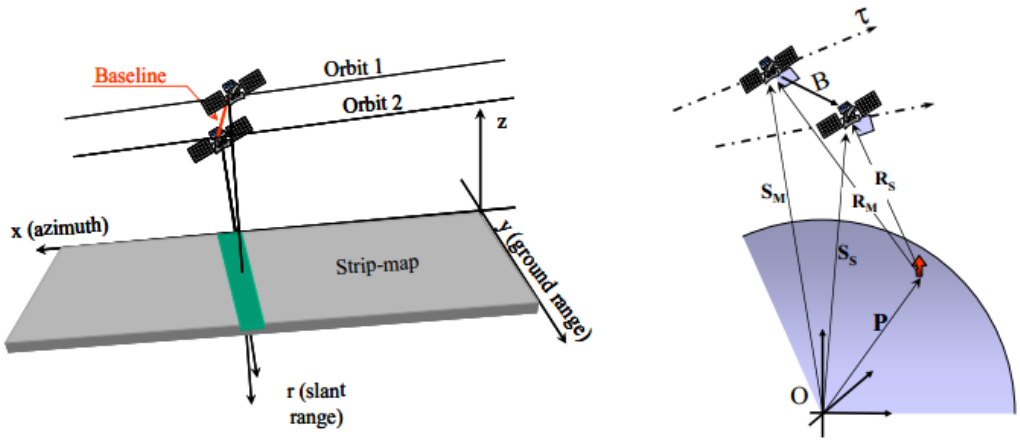

Figure 2.18: Interferometric SAR geometry

Chapter 3

Mathematical tools for the analysis of the time series

In the following chapter, the theoretical background needed in order to understand the basis of time series analysis aimed at classification, will be described.

In the first section all of the mathematical tools needed for the identification of the statistical properties of the time series will be provided.
In the second section a brief outline on the correlation between the time series and know meteorological events will be found.
Finally, in the last section, single and multiple step detectors will be discussed.

3.1 Mathematical tools for statistical properties identification

In order to assign a specific class to a pixel, the shape and statistical properties of its time series need to be thoroughly investigated. Different estimations are required to evaluate different characteristics.
Each mathematical tool description will be associated with its application on the time series related to the area of *Castello Sforzesco* depicted in the SAR image in Figure 3.1.

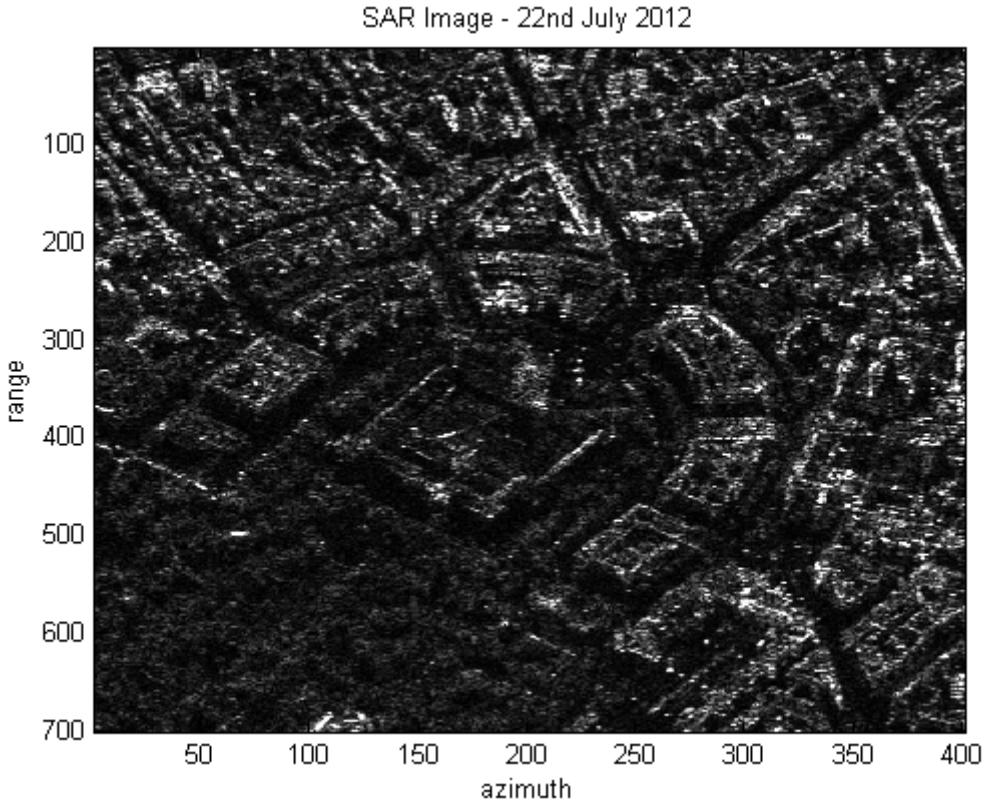

Figure 3.1: SAR image of *Castello Sforzeso*

3.1.1 Interferometric coherence

Coherence is a tool used in interferometry in order to measure the interferometric phase noise or as a means for image classification (stable scatterers such as buildings exhibit low phase noise, thus showing high coherence even between long time intervals).

The coherence γ between the two variables y_1 and y_2 is defined as:

$$\gamma = \frac{E[y_1 y_2^*]}{\sqrt{E[|y_1|^2]E[|y_2|^2]}} \tag{3.1}$$

Ideally the expected values are obtained using a set of observations for every pixel. Unfortunately, this is not feasible as often only two images are available.

In practical situations the accuracy of phase observations in a uniform region is assumed to be stationary. Under the assumption of ergodicity it is possible to exchange the ensemble averages with spatial averages obtained over a limited area. This assumption is used to calculate the maximum likelihood estimator of the coherence magnitude $|\widehat{\gamma}|$ over an estimation window of N pixels [9]:

$$|\widehat{\gamma}| = \frac{|\sum_{n=1}^{N} y_1^{(n)} y_2^{*(n)}|}{\sqrt{\sum_{n=1}^{N}|y_1^{(n)}|^2 \sum_{n=1}^{N}|y_2^{(n)}|^2}} \tag{3.2}$$

Coherence is subjected to a decorrelation that may originate from different noise sources. The main causes are geometric and temporal decorrelation:

- Geometric decorrelation. This is the result of the different angles of incidence between two different acquisitions;
- Temporal decorrelation. It occurs when a scatterer changes its electrical characteristics or its distribution between temporally spaced acquisitions.

In order to make these factors less influencing, coherence can be calculated by considering both time and space samples.
Using images that differ by a normal baseline of maximum 100m and a spatial average on a 5×5 pixel area, the interferometric coherence on a central area of Milan results as depicted in Figure 3.2:

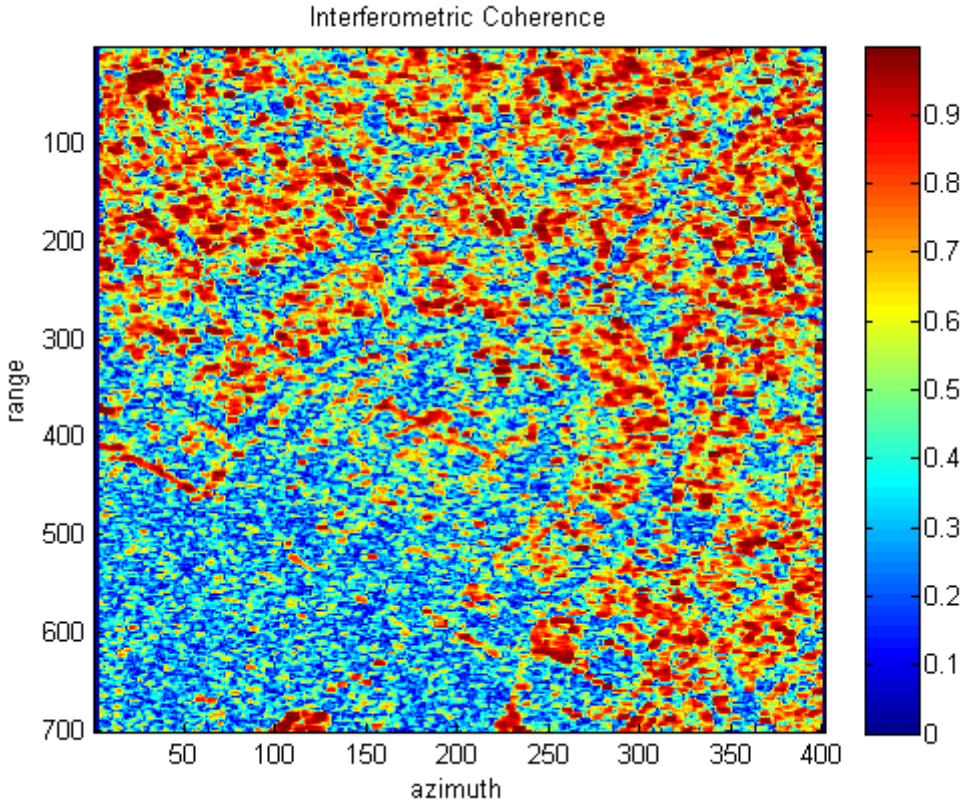

Figure 3.2: Interferometric coherence analysis on the *Castello Sforzeso*.

Referring to Figure 3.2, it can be easily confirmed that buildings exhibit high coherence values whereas vegetation pixels exhibit low coherence values.

3.1.2 Mean

The arithmetic mean of the amplitude of the time series of the k-th pixel can be calculated as:

$$\mu^k = \frac{1}{N} \sum_{n=1}^{N} p_n^k \tag{3.3}$$

Where p_n^k is the k-th pixel from the n-th image in the data-set.

Calculating now the temporal mean for the time series of every amplitude pixel in the *Castello Sforzesco* area, the results in Figure 3.3 can be obtained:

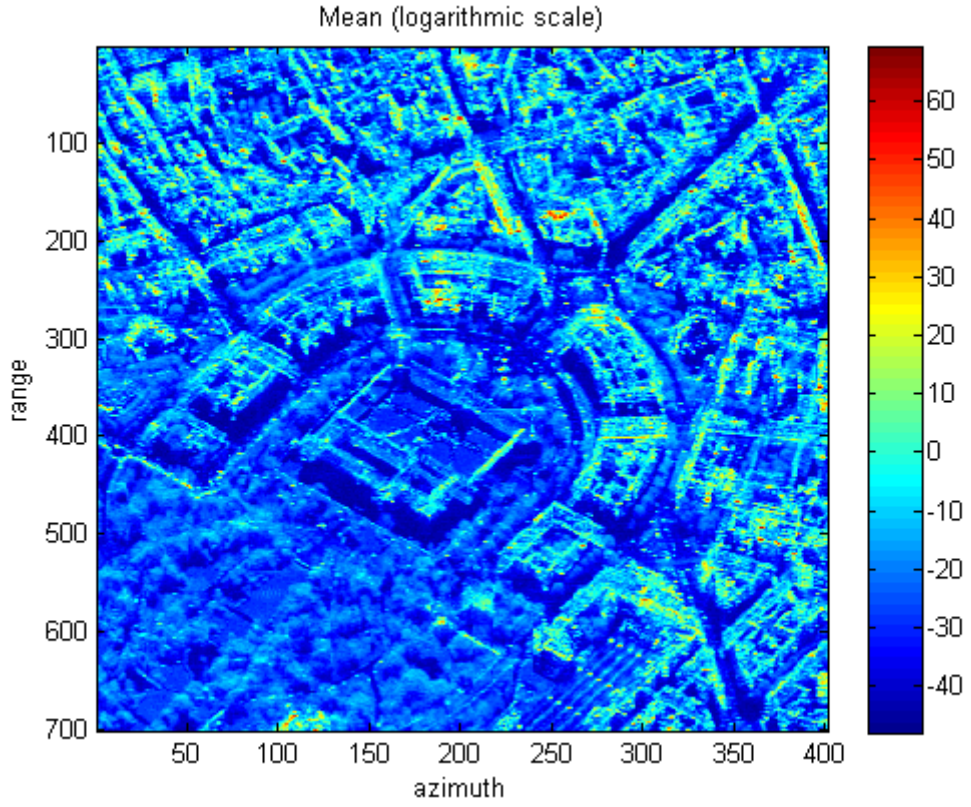

Figure 3.3: Temporal mean of *Castello Sforzeso*. The logarithmic scale is needed in order to properly visualize the data.

As it can be easily appreciated from Figure 3.3, by averaging the time series speckle disappeares, making the image become clearer. Also, buildings are characterized by higher averages with respect to vegetation and -obviously- shadow areas.

Furthermore, a logarithmic scale is absolutely necessary in order to properly visualize the data. This is a consequence of the fact that the mean amplitudes range from 0.091 to 32.2 and that the 90.6% of these values are included between 0.091 and 1.

3.1.3 Kurtosis

Kurtosis is a non-gaussianity test. Positive kurtosis indicates heavy tails and peakedness of the distribution (see Figure 3.5 on the left-hand side), whereas negative kurtosis indicates light tails and flatness of the distribution (see Figure 3.5 on the right-hand side) [10]. It is defined as:

$$K = \frac{\mu_4}{\sigma^4} \tag{3.4}$$

Where μ_4 is the fourth moment about the mean and σ is the standard deviation. Since the normal distribution has a kurtosis of 3, $K - 3$ is often used, so that the reference normal distribution has zero kurtosis.

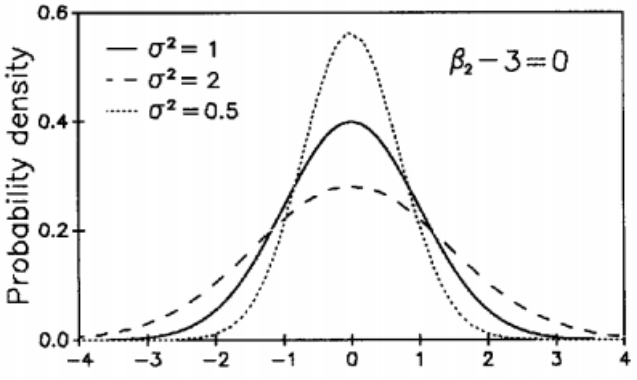

Figure 3.4: Normal distributions for different variances.

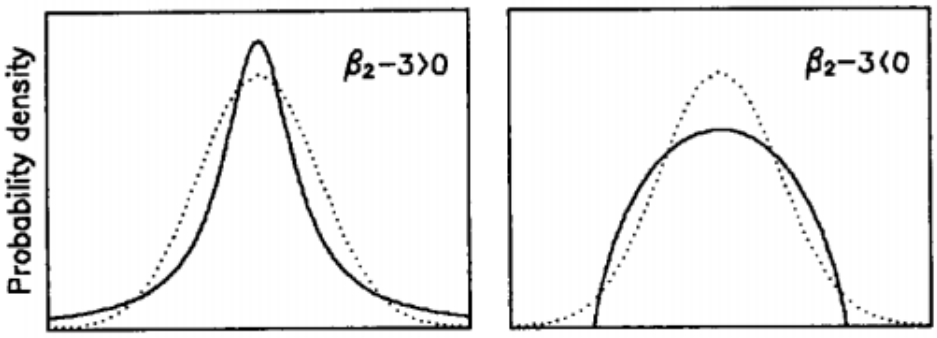

Figure 3.5: An illustration of different peaked and flat kurtosis. The dotted lines are the reference normal distribution.

Applying kurtosis on the same area previously evaluated, the results in Figure 3.6 can be obtained.

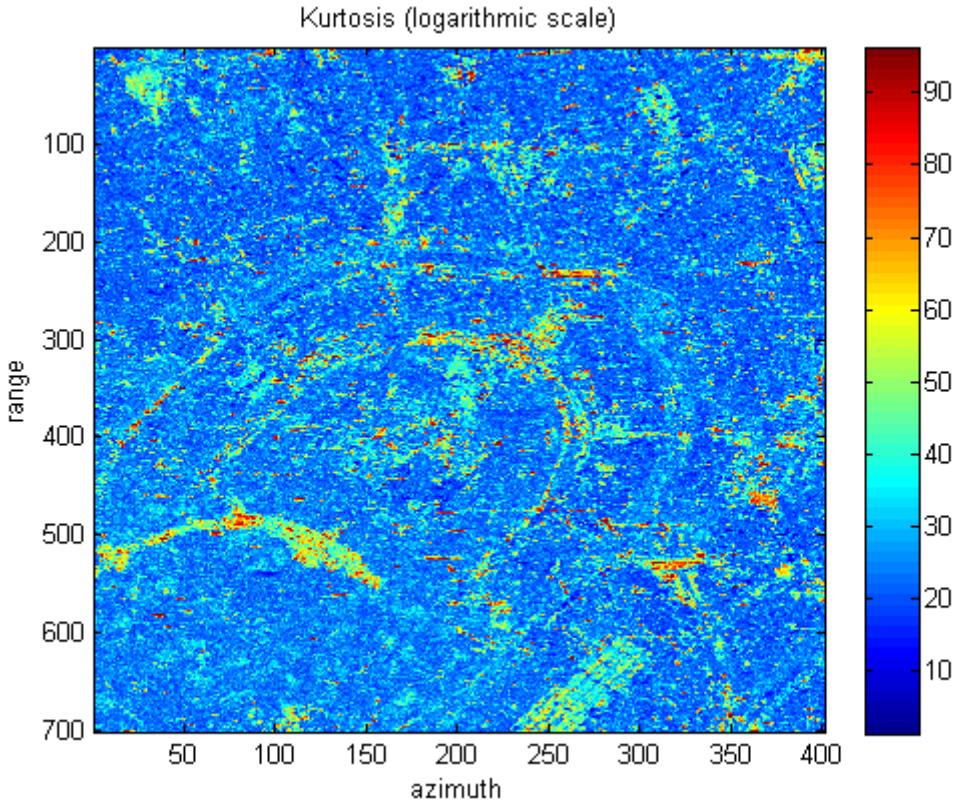

Figure 3.6: Kurtosis on *Castello Sforzeso*. The logarithmic scale is needed in order to properly visualize the data.

Again, a logarithmic scale is needed. Kurtosis values range from a minimum of 1.07 to a maximum of 123.5 and the 91.7% of its values are within the 1.07 - 10 range.

As it can be seen, kurtosis makes roads and pavements stand out. This peculiarity will be further discussed in section 4.2.1.2

3.1.4 Entropy

In information theory, entropy is a measure of the uncertainty associated to a random variable and it is defined as:

$$H(x) = -\sum_{x \in X} p(x) \log_2 p(x) \tag{3.5}$$

Where x is the random variable or, in our case, the time series. When applied to a SAR image, $p(x)$ is the probability of grayscale level. High entropy corresponds to high pixel variability and low entropy indicates stable pixels.

Estimating the entropy on the *Castello Sforzesco*, Figure 3.7 can be obtained.

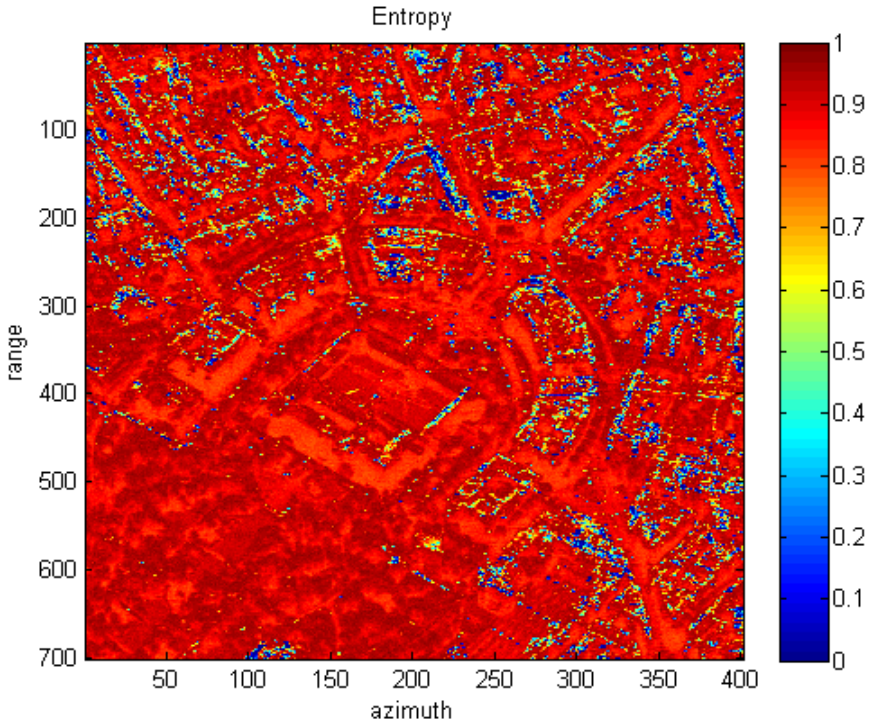

Figure 3.7: Normalized entropy on *Castello Sforzeso*.

Predictably, buildings are characterized by low entropy whereas vegetation has very high values.

3.1.5 Seasonal sinusoidal trend

Another statistical parameter that needs to be detected is the seasonal pattern. This can be modeled by a sinusoidal wave characterized by a 365-day period.

The received amplitude, which also depends on the scatterer's characteristics, can be therefore modeled by the following equation:

$$a = \alpha \sin\left(\frac{2\pi}{365}t + \varphi\right) + \beta \tag{3.6}$$

Where α and β are parameters that mainly depend on the shape and on the dielectric constant of the scatterer and the phase shift φ accounts for the fact that not every ground element with a seasonal component has seasonality peak in the same day/year period.

Once the model has been established, in order to evaluate the three unknown parameters, a Maximum Likelihood estimation has been implemented.

Aiming now at a linear model, the amplitude can be re-written as in equation 3.7:

$$a = \alpha \sin\left(\frac{2\pi}{365}t\right)\cos(\varphi) + \alpha \cos\left(\frac{2\pi}{365}t\right)\sin(\varphi) + \beta \tag{3.7}$$

Assigning now:

$$\alpha_1 = \alpha \cos(\varphi) \tag{3.8}$$
$$\alpha_2 = \alpha \sin(\varphi) \tag{3.9}$$

We obtain:

$$a = \alpha_1 \sin\left(\frac{2\pi}{365}t\right) + \alpha_2 \cos\left(\frac{2\pi}{365}t\right) + \beta \tag{3.10}$$

Which in matrix form, can be written as:

$$\mathbf{A} = \begin{bmatrix} \sin\left(\frac{2\pi}{365}t\right) & \cos\left(\frac{2\pi}{365}t\right) & 1 \end{bmatrix} \begin{bmatrix} \alpha_1 \\ \alpha_2 \\ \beta \end{bmatrix} = \mathbf{H}\boldsymbol{\theta} \tag{3.11}$$

The Maximum Likelihood estimates the parameters with:

$$\hat{\boldsymbol{\theta}}_{ML} = \left(\mathbf{H}^T\mathbf{H}\right)^{-1}\mathbf{H}^T\mathbf{x} \tag{3.12}$$

Where the matrix $\mathbf{x}$ is the amplitude's time series.

The results of the ML estimation are represented in Figure 3.8.

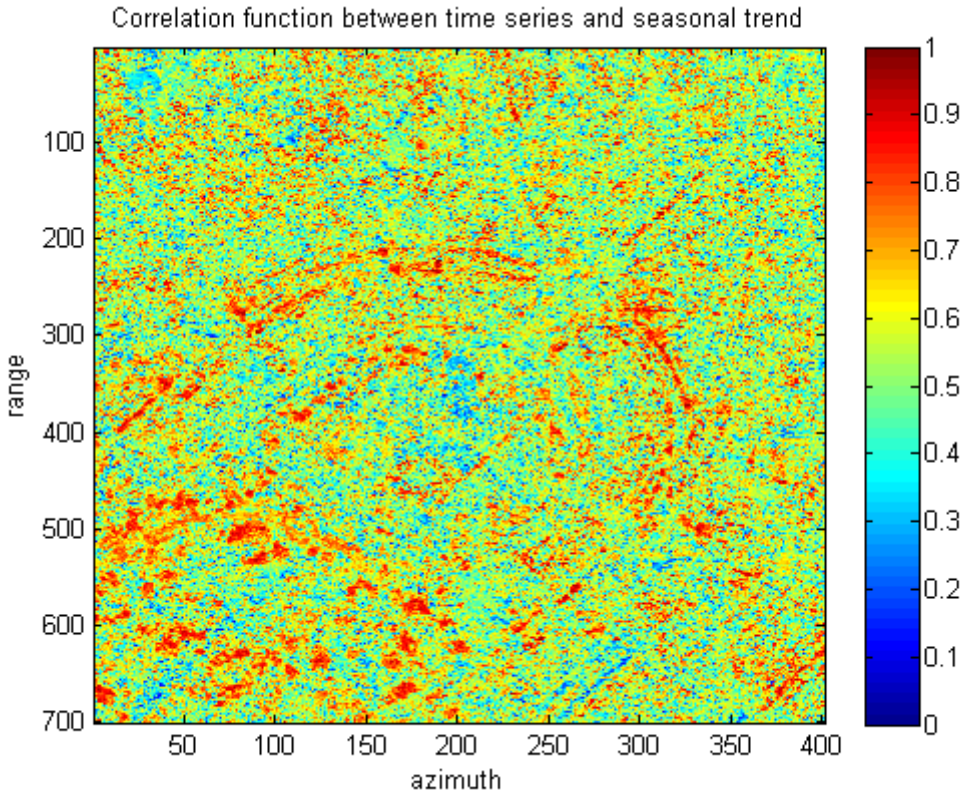

Figure 3.8: Correlation function between time series and seasonal trend.

As it can be seen, the highest values of correlation correspond to vegetated areas and tree-lined roads.

In order to validate the previous calculations and confirm that an actual sinusoidal trend has been fitted and not just random noise, the ratio between the sine's amplitude and the error's standard deviation (e.g. the standard deviation of the difference between the seasonal sine function and the real data) needs to be evaluated.

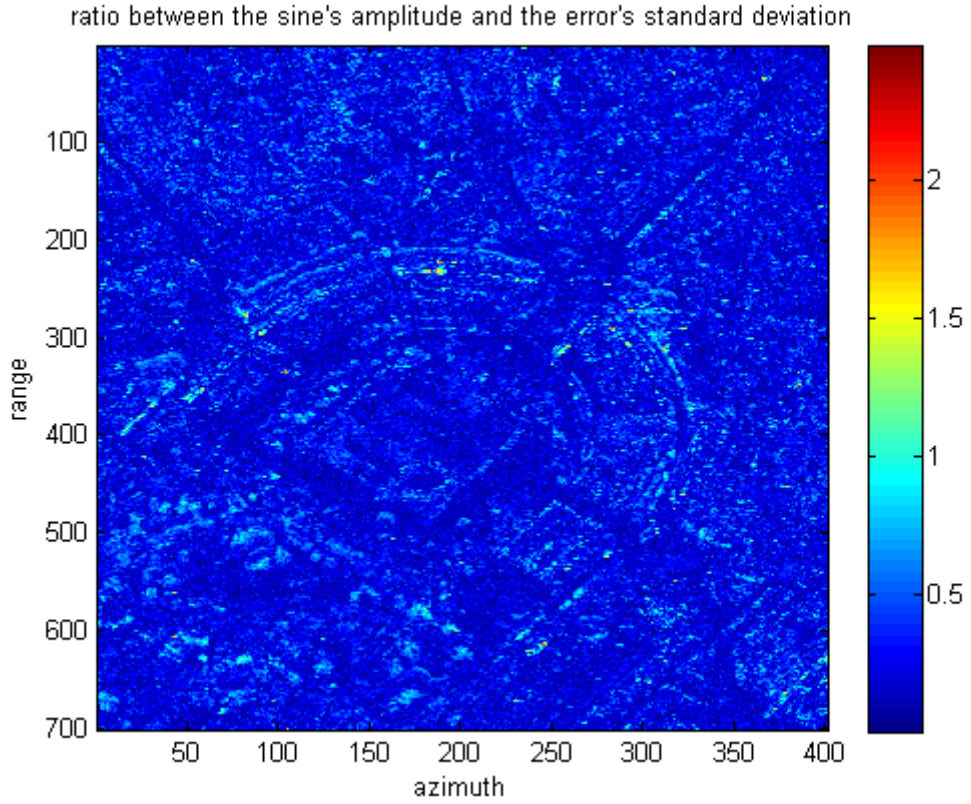

Figure 3.9: Ratio between the seasonal sine wave's amplitude and the error's standard deviation.

As it can be seen in Figure 3.9, this ratio maintains very low values, even for pixels that are known to have a real sinusoidal trend (such as vegetation pixels).

In order to justify this fact, the abovementioned ratio versus the correlation function has been plotted in Figure 3.10:

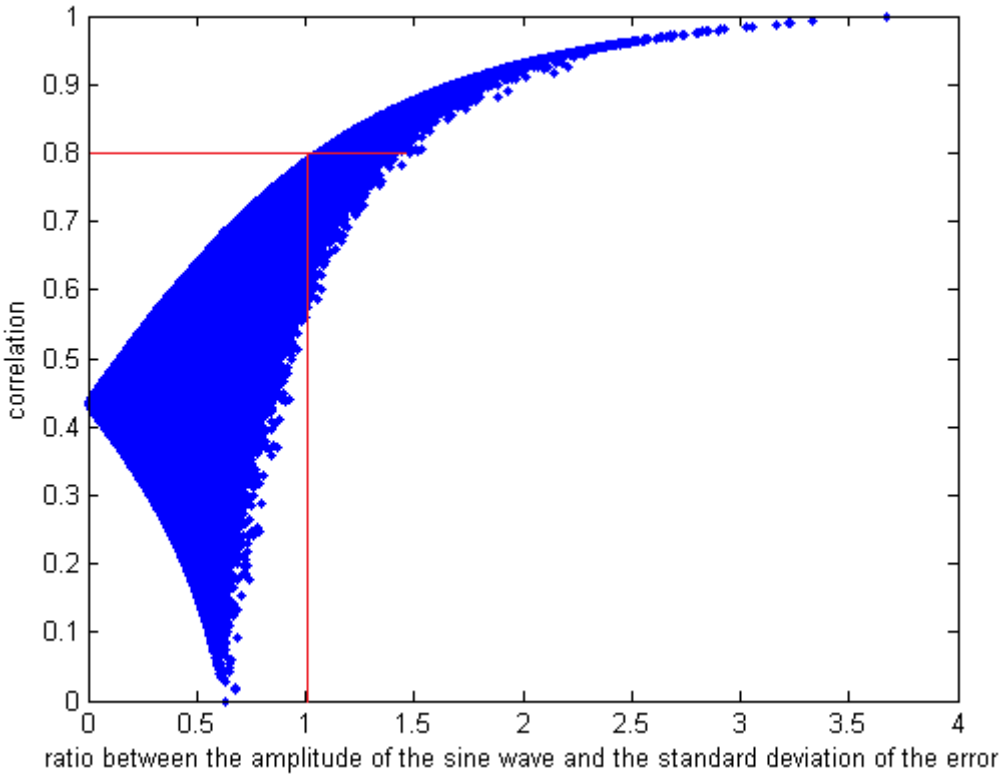

Figure 3.10: A/σ versus correlation function.

According to this plot, to high values of correlation correspond high values of A/σ.

This validates the results in Figure 3.8 and leads to a very careful consideration about the reasons why Figure 3.9 is characterized by such a low average: due to the fact that A is the amplitude that best fits *all* of the six available years and not the actual signal strength, A/σ is not a signal-to-noise ratio.

This distinction can be easily understood with the aid of the Figure 3.11 that represents both the seasonal trend characterized by amplitude A and the actual time series of the pixel.

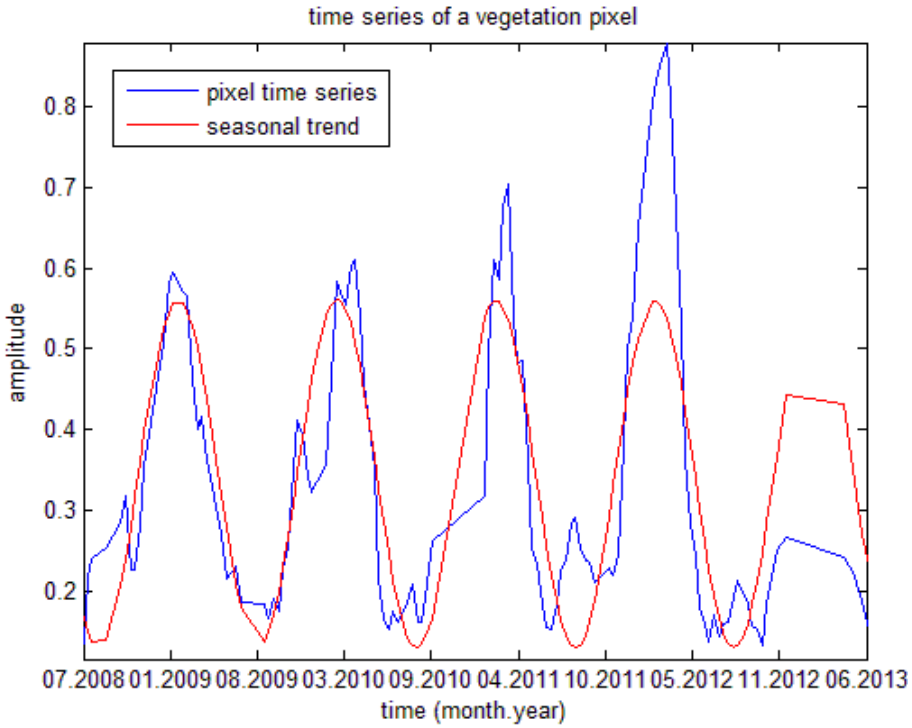

Figure 3.11: Comparison between seasonal trend and time series.

As it can be seen in the example in Figure 3.11, the standard deviation of the difference between seasonal trend and pixel's time series will be therefore averaged between the very low values corresponding to the first years and the very high values corresponding to the last years.

Due to these discrepancies between years, the ratio A/σ is not going to be very high.

Keeping in mind all of the above considerations, it can be seen that Figure 3.10 also provides the means to establish a threshold to separate valid and invalid pixels: correlation functions higher or equal to 0.8 grant a A/σ ratio higher than 1.

3.2 Correlation to known meteorological events

In order to establish a connection between the amplitude of the pixel and registered meteorological events such as temperature, humidity or rain, a correlation function -very similar to the one implemented for the seasonal case- can be evaluated.

As part of this study, the correlation between the time series and temperature data has been estimated.

Firstly, in order to calculate the parameters α and β, the meteorological data has been modelled:

$$\mathbf{A} = \begin{bmatrix} m(t) & 1 \end{bmatrix} \begin{bmatrix} \alpha \\ \beta \end{bmatrix} = \mathbf{H}\boldsymbol{\theta} \tag{3.13}$$

Where $m(t)$ is the day-by-day average of a specific meteorological event registered by a certain weather station. Finally, the Maximum Likelihood estimation has been implemented:

$$\hat{\boldsymbol{\theta}}_{ML} = \left(\mathbf{H}^T\mathbf{H}\right)^{-1}\mathbf{H}^T\mathbf{x} \tag{3.14}$$

A time-shift of the temperature data has been considered. However, most of the estimations requested a negative time-shift, showing therefore a stronger correlation to a general sinusoidal trend rather than a specific temperature trend (this fact can be also confirmed in the comparison in Figure 3.12). Due to this reason, no time-shift has been ultimately implemented.

Analyzing now the temperature data originated in the weather station *Milano Linate* and selecting the region within the available data-set closest to such station, the results in Figure 3.12 can be obtained.

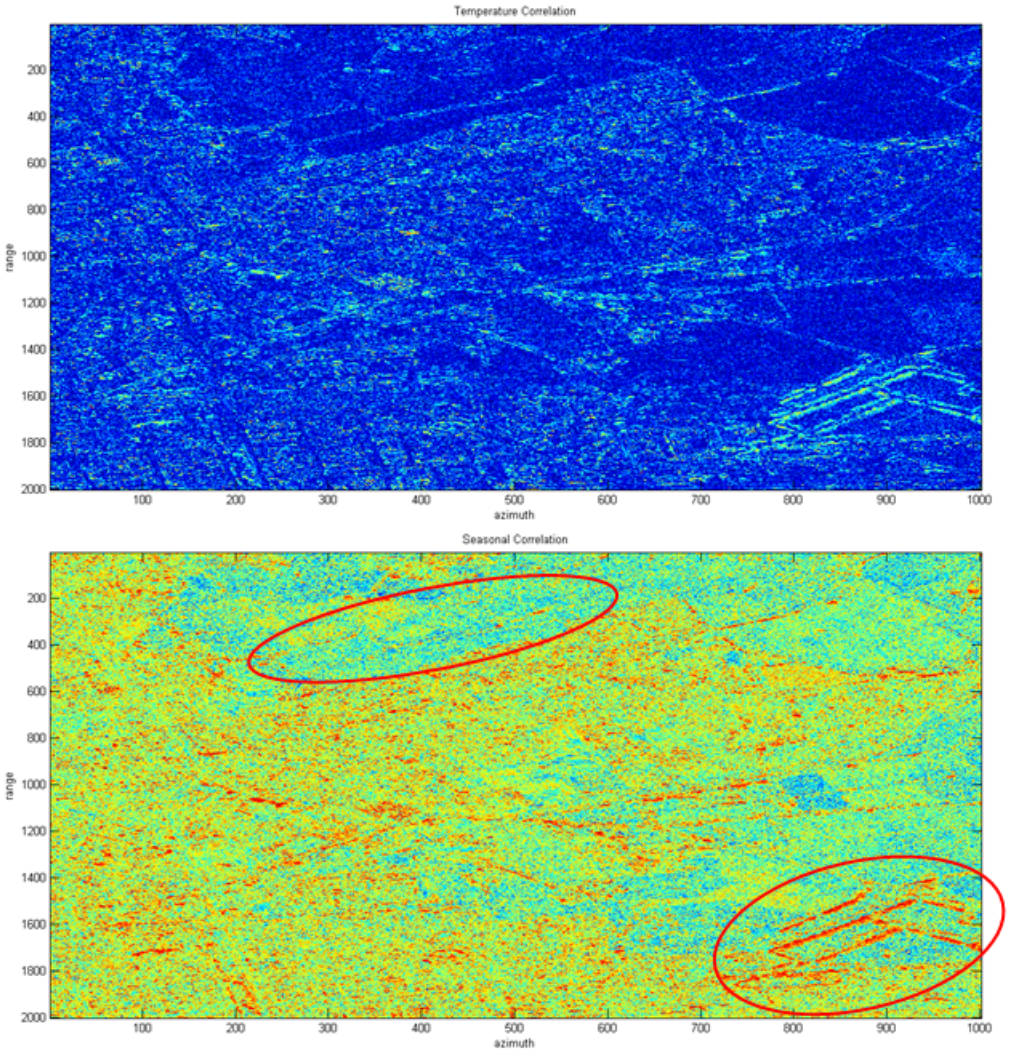

Figure 3.12: Temperature and seasonal correlation in the south-east area of Milan. Circled in red are the areas where the two estimations differ the most.

For comparison, both the temperature and the seasonal correlations have been implemented on the same area. The importance of this juxtaposition lies on the fact that the temperature varies according to the season and it could be therefore hypothesized that no additional information could be drawn by such correlation.

As it can be observed, this is not true. Circled in red are areas where an important difference between temperature and seasonal correlations can be acknowledged.

This fact, though, has not been additionally analyzed and therefore no conclusions have been drawn on the reasons that led to such variations. This could constitute a very interesting further development.

3.3 Change detection

Change detection is an image processing technique that allows the detection of changes that occur in a given monitored area between successive acquisitions. Each ground modification will be seen by the radar as a transition step in the time series. A step is an abrupt variation in the amplitude that lasts for more than one neighboring samples. Steps can be single or multiple according to the number of transitions that occur in the time series.

Change detection varies greatly according to the selected literature. It differs in:

- Used data type:
  - Coherent change detection - uses the phase info contained in the SAR image;
  - Incoherent change detection - uses the amplitude info in the SAR image;
- Threshold selection:
  - Supervised;
  - Automatic - aimed at discriminating between classes without any prior knowledge about the scene.
- Estimator: in case of automatic threshold selection, many different estimators can be found.

The step detector that has been hereby considered uses the information contained in amplitude time series has an automatic threshold selection and uses a Bayesian estimator.

3.3.1 Single step detection

The single step within a time series can be modeled as follows (see Figure 3.13):

$$d_i = \begin{cases} \mu_1 + n_1(i) & \text{if} \quad x \leq m \\ \mu_2 + n_2(i) & \text{if} \quad m+1 \leq k \leq N \end{cases} \tag{3.15}$$

Where d_i is the data under analysis (e.g. the time series of the amplitude), μ_1 and μ_2 are the two constant amplitudes, $n_1(i)$ and $n_2(i)$ is the additive noise

(modelled as white Gaussian noise), N is the length of the time series and m the position of the step.

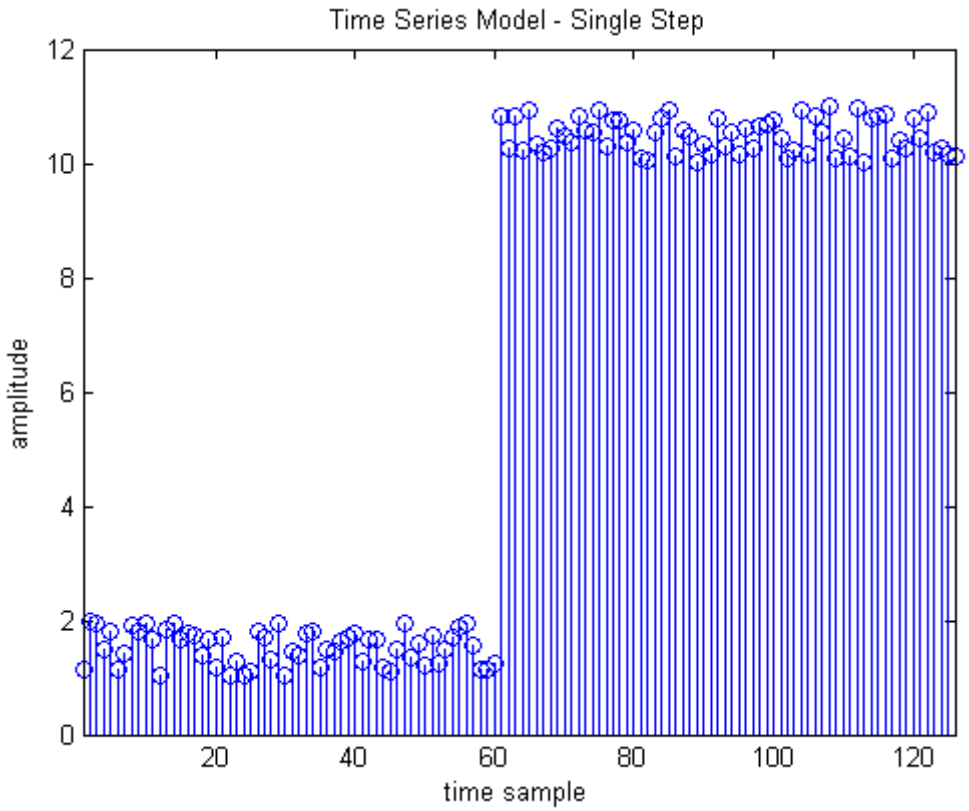

Figure 3.13: Time series model for single step detection.

Bayes's Theorem is a statistical formula that states that the *conditional probability* of x given y, equals to the *joint probability* of x and y, divided by the *prior probability* of y:

$$p(x|y) = \frac{p(x,y)}{p(y)} = p(x)\frac{p(x|y)}{p(y)} \tag{3.16}$$

This theorem, applied to inverse problems, is a very important tool that enables the estimation of the statistical model described by Equation 3.17:

$$p(\mathbf{m}|\mathbf{d}) = p(\mathbf{m})\frac{p(\mathbf{d}|\mathbf{m})}{p(\mathbf{d})} \tag{3.17}$$

The probability of the model given the data (e.g. the *posterior distribution*), equals to the *prior distribution* of the model, multiplied by the probability of the data given the model (e.g. the *likelihood* which refers to past events that provided known results and is the direct problem), divided by the *prior distribution* of the data.

It also needs to be observed that $p(\mathbf{d})$ does not depend on the model and can therefore be considered constant. Hence, the likelihood-based inversion can be finally

re-written as [11]:

$$p(\mathbf{m}|\mathbf{d}) \propto p(\mathbf{d}|\mathbf{m})p(\mathbf{m}) \tag{3.18}$$

Applying the single step model to the Bayesian estimator, the following result can be obtained [12]:

$$p(\{m\}|\mathbf{d},\mathbf{I}) \propto \frac{1}{\sqrt{m(N-m)}} \times \left[\sum_{i=1}^{m} d_i^2 - \frac{1}{m}\left(\sum_{i=1}^{m} d_i\right)^2\right]^{-\frac{m-2}{2}} \times \left[\sum_{k=m+1}^{N} d_k^2 - \frac{1}{N-m}\left(\sum_{k=m+1}^{N} d_k\right)^2\right]^{-\frac{N-m-2}{2}} \tag{3.19}$$

Evaluating with the above estimation an area characterized by newly constructed buildings (specifically, the area of *piazza Gae Aulenti* and *Porta Nuova*), the result in Figure 3.14 can be obtained:

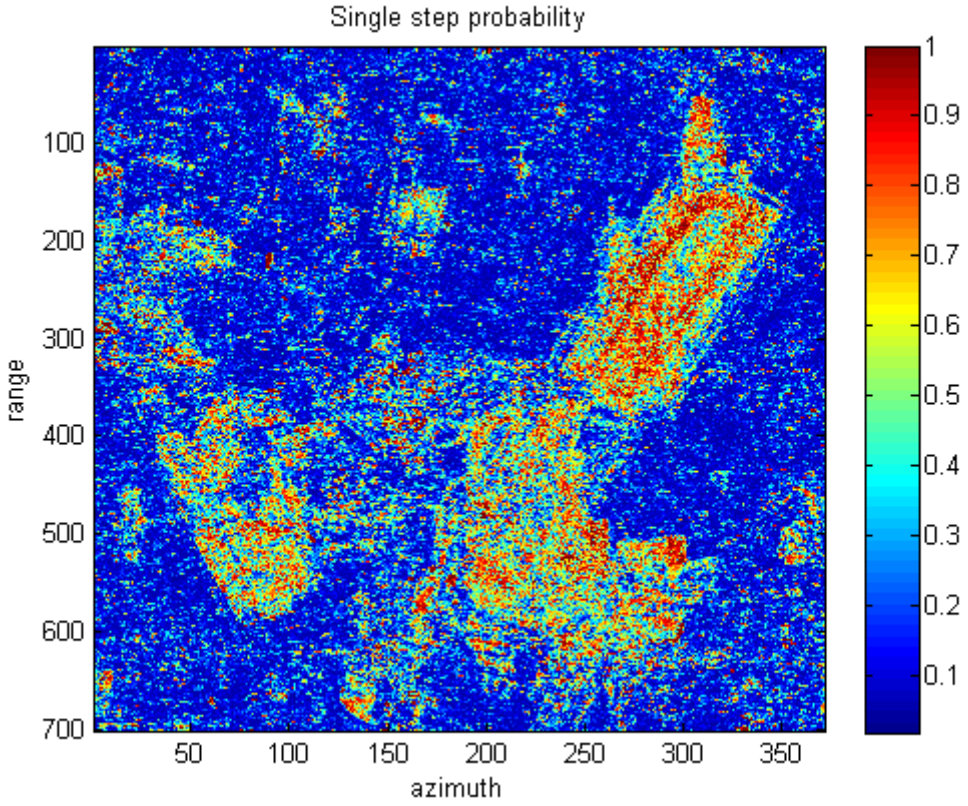

Figure 3.14: Single step probability function on an area characterized by newly constructed buildings.

As it can be seen, the pixels corresponding to the areas where new buildings have been constructed are characterized by very high step probability.

3.3.2 Multiple step detection

The single step model can be extended to multiple steps. In case of double step, the model is as follows (see Figure 3.15):

$$d_i = \begin{cases} \mu_1 + n_1(i) & \text{if} \quad i \leq m \\ \mu_2 + n_2(i) & \text{if} \quad m+1 \leq k \leq l \\ \mu_3 + n_3(i) & \text{if} \quad l+1 \leq k \leq N \end{cases} \tag{3.20}$$

Where d_i is the data under analysis, μ_1, μ_2 and μ_3 are the constant amplitudes, $n_1(i)$, $n_2(i)$ and $n_3(i)$ is the additive noise (modelled as white Gaussian noise), N is the length of the time series and m and l are the positions of the two steps.

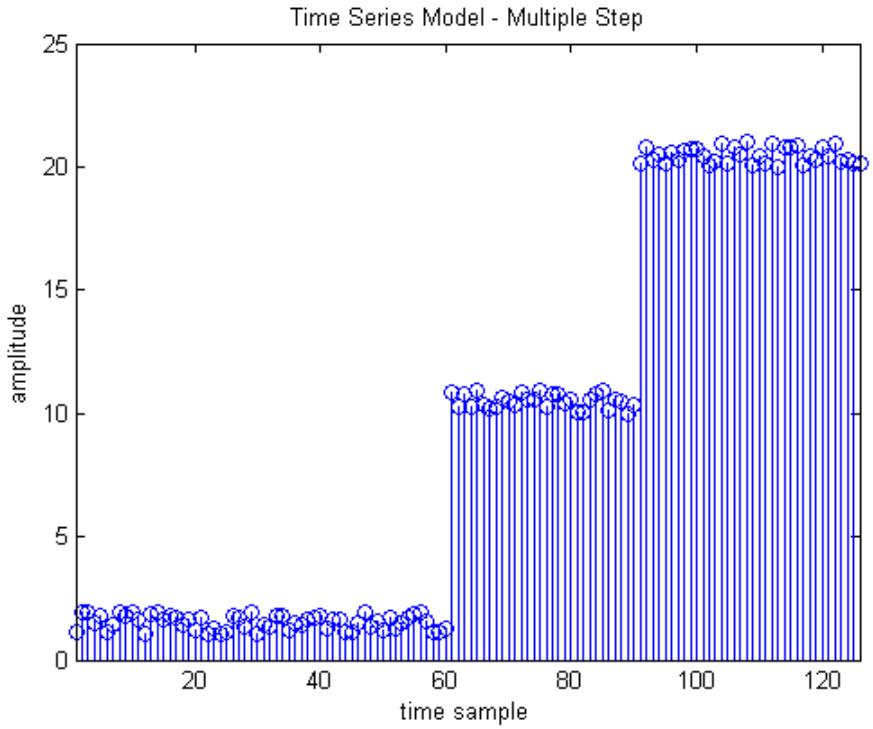

Figure 3.15: Time series model for double step detection.

With the additional step the Bayesian estimator becomes:

$$\begin{aligned} p(\{m\}|\mathbf{d},\mathbf{I}) \propto \frac{1}{\sqrt{m(l-m)(N-l)}} \quad & \times \quad \left[\sum_{i=1}^{m} d_i^2 - \frac{1}{m}\left(\sum_{i=1}^{m} d_i\right)^2\right]^{-\frac{m-2}{2}} \\ & \times \quad \left[\sum_{k=m+1}^{l} d_k^2 - \frac{1}{l-m}\left(\sum_{k=m+1}^{l} d_k\right)^2\right]^{-\frac{l-m-2}{2}} \\ & \times \quad \left[\sum_{p=l+1}^{N} d_p^2 - \frac{1}{N-l}\left(\sum_{p=l+1}^{N} d_p\right)^2\right]^{-\frac{N-l-2}{2}} \end{aligned} \tag{3.21}$$

Analyzing now with the double step detector the same area previously considered, the Figure 3.16 can be obtained:

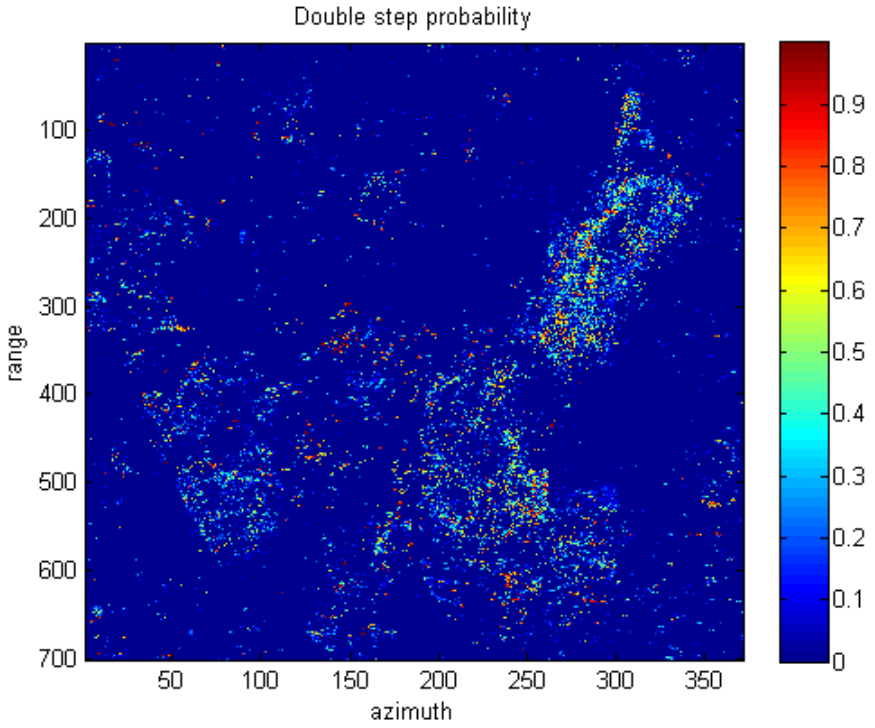

Figure 3.16: Double step probability function on an area characterized by newly constructed buildings.

Given the fact that the number of pixels that exhibit a double step is smaller than the number of pixels that present a single step (e.g. all of the pixels that have a double step also have a single step), the average probability for the double step detection in Figure 3.16 is considerably smaller than the one for the single step detection depicted in Figure 3.14.

Triple and quadruple step detectors have also been taken into account and implemented. However, due to the fact that they provided only marginal information at the price of extremely time and memory-consuming algorithms, they will be hereby discarded.

Chapter 4

Classification results

All of the results achieved with the classification and change detection algorithms will be described in this chapter.

Firstly, an introduction of the area under investigation and related data-set has been outlined, followed by the description of how the time series analysis has been implemented.
In the third paragraph three types of classification have been described: one obtained with interferometric coherence, another with the standard classification algorithm hereafter proposed and finally one related to change detection considerations.
In the conclusive paragraph two peculiarities that might cause issues if not carefully evaluated have been discussed.

4.1 The data-set and the area under investigation

In order to select an area that enclosed all of the characteristics under investigation, images of the entire city of Milan have been analyzed.

The study region, that covers approximately 76km^2, comprises old stable buildings, newly constructed buildings, parks gardens and fields, sport centers and arenas, roads and squares and a 500m long lake. For encompassing all of these characteristics, this area was identified as ideal for testing new classification and step detection algorithms.

The equivalent SAR satellite image is composed of 5100 pixel with a ground resolution of 1.5m in the range direction and of 5000 pixel with a ground resolution of 2m in the azimuth direction.

In order to check the effectiveness of the various compilers, specific emphasis has been placed on distinctive neighborhoods around the city.

Initially, during the stage of detection and tracking of newly constructed buildings, *piazza Gae Aulenti* and the area of *Porta Nuova* were analyzed. The aforementioned quarter has been subject to an urban redevelopment project that began in 2005 and is partially ongoing and comprises the public square *piazza Gae Aulenti*, a part of the business district, public offices from the *Regione Lombardia*, private residences

and green areas.

During a later stage, as the effectiveness of the algorithm in extra-urban areas had been tested, the *Parco Agricolo Sud Milano* has been observed. This is a green reserve, protected by the *Regione Lombardia*, which is characterized by crops, woods as well as water streams and ponds.

Finally, a classification of the entire city was undertaken.

For the purpose of time-series analysis, 126 images acquired by the TerraSAR-X satellite between the 17th of February 2008 and the 20th of July 2013 have been considered. These images were not evenly spaced however, without considering the initial and final acquisition years, were characterized by an average of 27 images per year.

Furthermore, the images of the data-set, which were all acquired along a descending orbit and are HH-polarized, were subjected to power calibration during a later processing stage.

4.2 Time series analysis

As mentioned in the introductory chapter, the key innovation on which this thesis is based is the exploitation of the pixel's time series, aimed at a high resolution classification.

A variety of forms of time series analysis have been performed depending on whether the algorithm was classification-oriented or change detection-oriented.

Naturally, the time series is an effective approach only with the provision of a sufficient number of samples. As the time samples decrease, the classification algorithm is likely to encounter problems, especially with road and vegetation identification. Further details will be provided in the specific paragraphs.

4.2.1 Classification oriented

The time series analysis aimed at classification, assigns to the single pixel, one of four possible categories: building, road, vegetation and un-classified. The estimation is based on statistical parameters.

4.2.1.1 Time series of buildings pixels

Urban areas are characterized by a very strong backscatter. This is a consequence of the fact that, to the radar, buildings are an ensemble of flat plates and, most importantly, corner reflectors which, due to their shape, convey a vast amount of energy back towards the satellite. Also, within an urban environment, numerous metallic objects such as antennas, balustrades, lamp poles and vent gratings can be found.

Due to these factors, building pixels can be identified by an amplitude that stands

out with respect to the other pixels.

In the following study the threshold has been set to the 45% of the amplitude dynamics on a logarithmic scale of the whole area.

This value, as all of the other values that will be later discussed (with the exception of the threshold of the correlation between time series and sinusoidal trend which has been discussed in section 3.1.5), has been selected by supervising the experimental results. Following the considerations previously made, it may seem low. However, it must be taken into account that in some specific areas the pixel amplitude can rise to extremely high values due to optimal geometry. These spikes result in the average building amplitude being inevitably lower.

In order to produce a more robust estimation, a second parameter has been considered. This further criteria is marked by low entropy. This is a consequence of the fact that the fixed geometry of the building does not allow a highly random behavior.

The threshold of entropy has been set to 80% of the entropy's dynamic in order to account for speckle and other elements that may introduce randomness into the time series. This inevitable component can be appreciated in Figure 4.1 which depicts the time series of a building pixel:

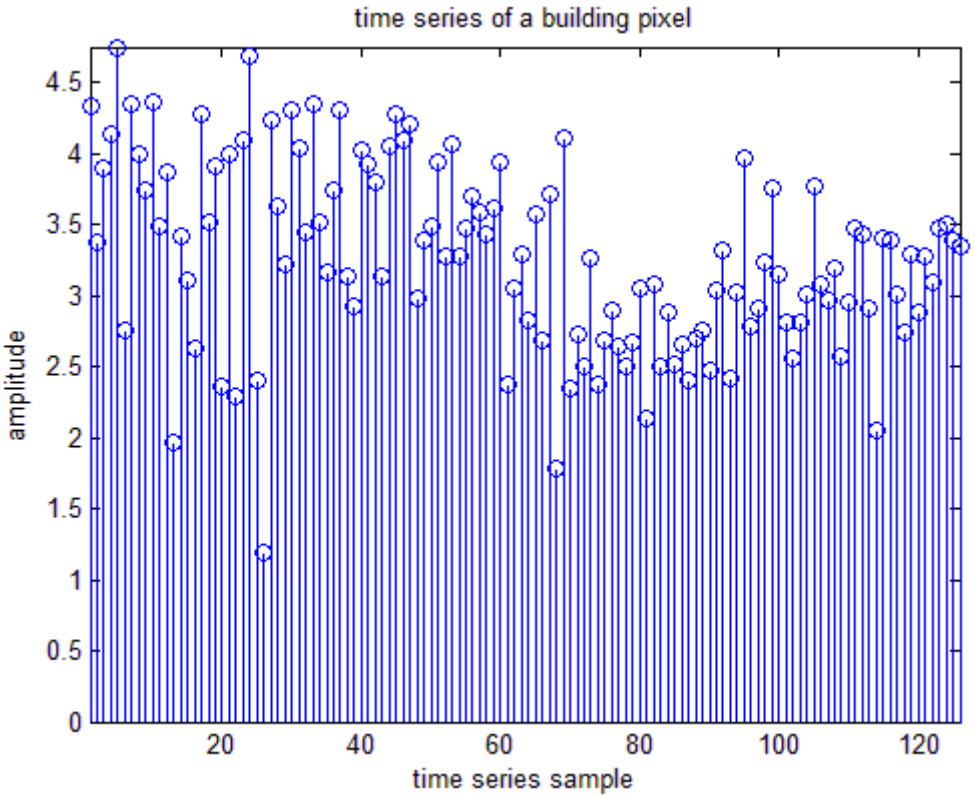

Figure 4.1: Time series of a building pixel.

4.2.1.2 Time series of road and square pixels

Roads and squares are characterized by a very low backscatter that can, at times, be disturbed by a very high spike. This is a consequence of the fact that these are usually flat areas with a relatively low dielectric constant (asphalt's constant is averagely $\varepsilon_{asphalt} \cong 6$) that nevertheless hold a large amount of randomness due to cars, road works, public events etc.

In the following study, in order to identify road and square pixels three thresholds have been considered:

- The mean of the time series must be lower than 45% of the mean amplitude dynamics on a logarithmic scale;
- The entropy of the time series must be higher than 80% of the entropy dynamics;
- The kurtosis of the time series must be higher than 62% of the kurtosis dynamics on a logarithmic scale.

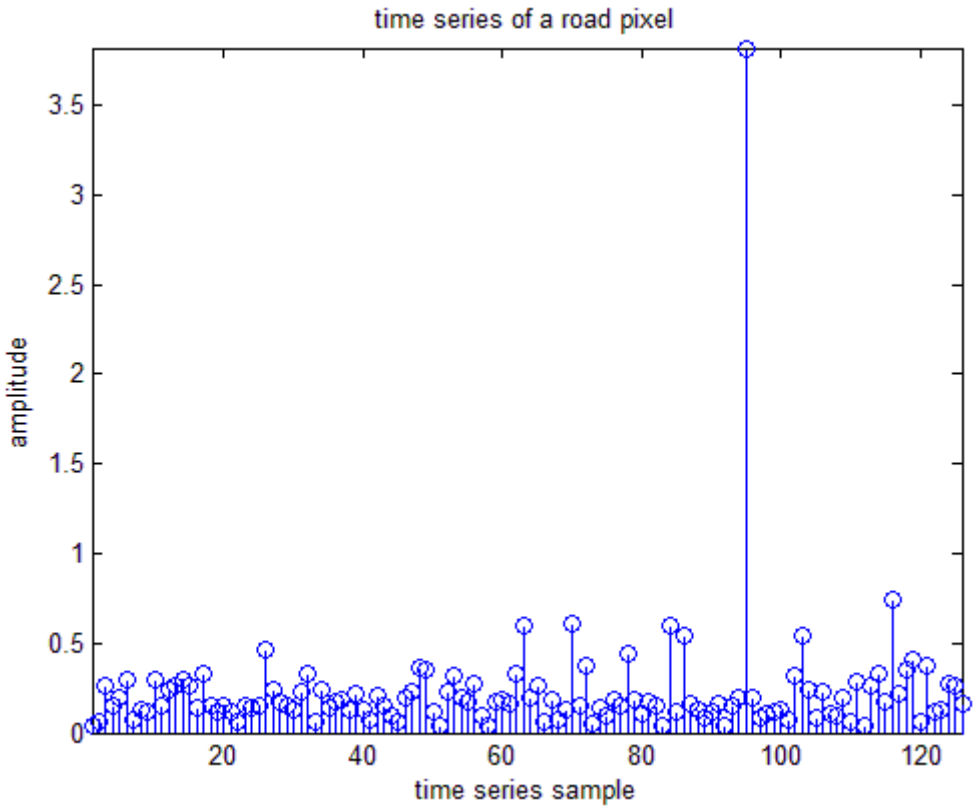

Figure 4.2: Time series of a road pixel.

As it appears clear from Figure 4.2, the greater the length of the time series, the higher the probability of detecting the spike(s) that will allow a correct classification. As the time series shrinks, roads are likely to disappear from classification.

4.2.1.3 Time series of vegetation pixels

Vegetation pixels can be characterized by different types of backscatter according to the type of crop.

4.2.1.3.1 Times series of grassland pixels Grassland and fields are difficult to identify based on the abovementioned statistics because they tend to have a very low backscatter that does not distinguish itself from the one originated by other elements such as sand or unused pavements. To overcome this limitation, a rough pre-processing of the area has been implemented based on an interferometric coherence algorithm, aimed at deleting all of those pixels from the area under investigation.

This simplification does not in any way diminish the validity of the classification algorithm, since fields are not considered an item of interest towards the purpose of urban sprawl monitoring. In the event that a building should be constructed in an area that had been assigned to a field, this would be identified by the step detector and subsequently placed again in the urban area under investigation.

4.2.1.3.2 Time series of tree pixels Given the fact that TerraSAR-X operates in the X-band, trees and bushes are particularly easy to recognize, with a combination of the statistical properties already considered and the correlation with a seasonal sinusoidal trend. This is due to the fact that a wavelength of 3.1cm cannot penetrate the canopy and the difference between a leaved tree and a bare one will be detected.

It needs to be highlighted that the peak of the seasonal trend will be in winter (as in the example in Figure 4.3), in some rare cases during spring and almost never in summer or autumn since leaves have a lower backscatter than the terrain and corner reflectors that will appear to the radar after the leaves have fallen from the branches.

In the following work, in order to identify vegetation pixels, three thresholds have been considered:

- The mean of the time series must be lower than 45% of the mean amplitude dynamics on a logarithmic scale;
- The entropy of the time series must be higher than 80% of the entropy dynamics;
- The correlation of the time series with a seasonal sinusoidal function must be higher than 80%;
- The phase-shift of the seasonal sinusoidal function must be positive (so that its peak will be during colder seasons).

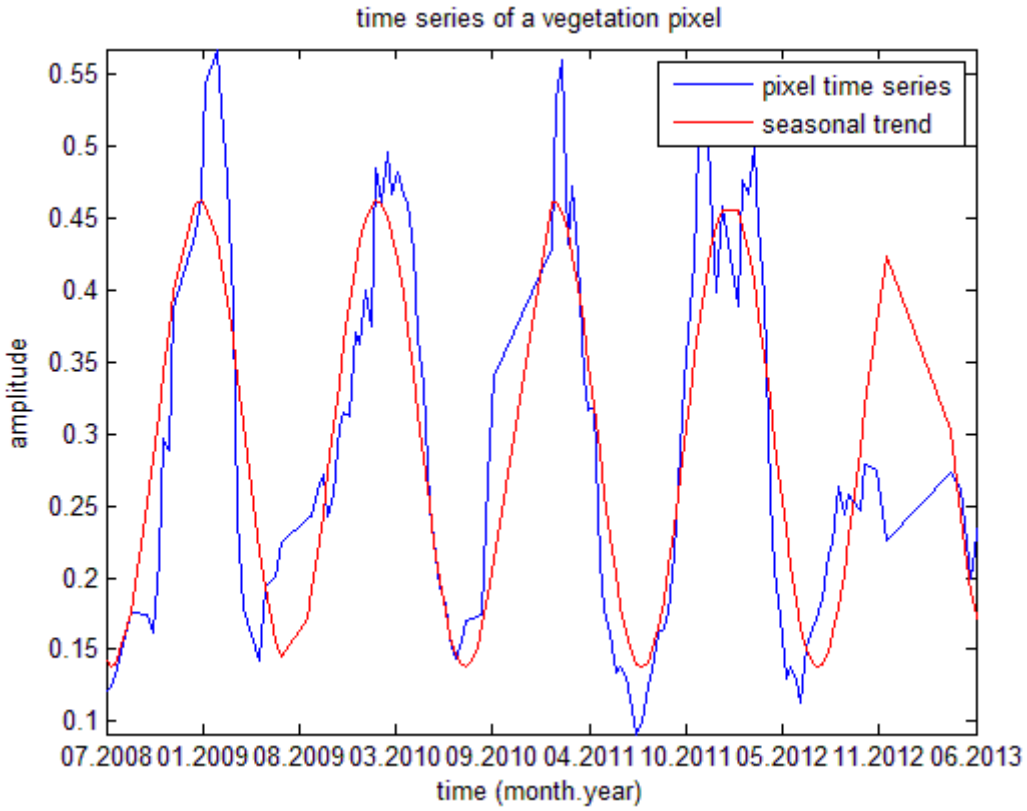

Figure 4.3: Time series of a vegetation pixel.

Naturally, the fewer the samples, the more imprecise the estimation will be. Unlike the road statistics, it is not just a matter of overall length but also of samples per year. In the event that an insufficient number of images were to be available, the ML estimation would still try to fit the pixel's time series into a sub-sampled seasonal trend, resulting in a rising number of false positives (e.g. there will be no real high correlation to compare with, leading to buildings misinterpreted as vegetation).

During the stage of vegetation identification, it is interesting to notice how specific trees and crops are characterized by a specific phase shift in the seasonal sinusoid. Despite the fact that this phenomenon is easier to identify with crops than with trees (since field growth, harvesting and tilling tend to be very specific according to the type of plant), an outstanding case has been found within the Milanese area.

As depicted in the Figure 4.4, the tree-lined road *via Marco de Marchi* can be noticed by the naked-eye because of its lower phase shift (approximately $\phi_{MdM} = 0.53$rad) compared to the average of the trees in the *Giardini Pubblici Indro Montanelli* (approximately $\phi_{GPIM} = 1.3$rad) that can be seen just higher up in the image.

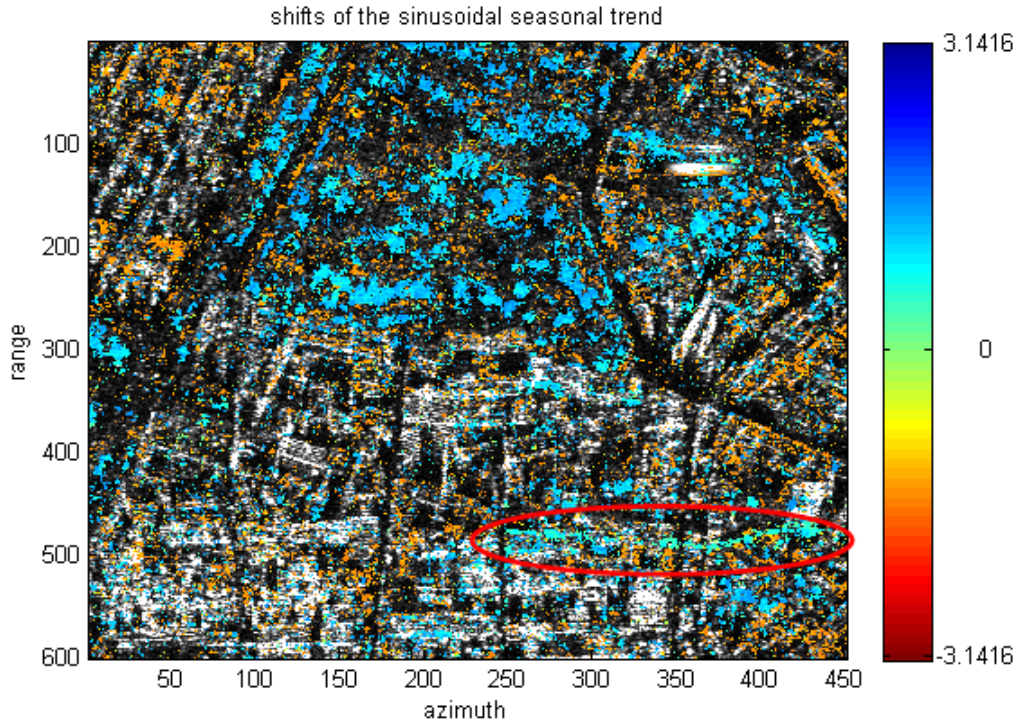

Figure 4.4: The tree-lined *via Marco de Marchi*. As it can be seen by the naked-eye, it is characterized by a lower phase-shift than the trees in the park above.

Comparing this result with images from Google Earth it can be confirmed that the trees that have been planted in *via Marco de Marchi* (Figure 4.5 on the left-hand side), differ from the ones in the *Giardini Pubblici Indro Montanelli* (Figure 4.5 on the righ-hand side).

Figure 4.5: Visual confirmation of the differences between the tree-lined road and the park.

Another interesting comparison can be made considering to which seasonal peak corresponds the phase shift. As it can be seen in Figure 4.6, *via Marco de Marchi* distinguishes itself as one of the unique points displaying a spring peak.

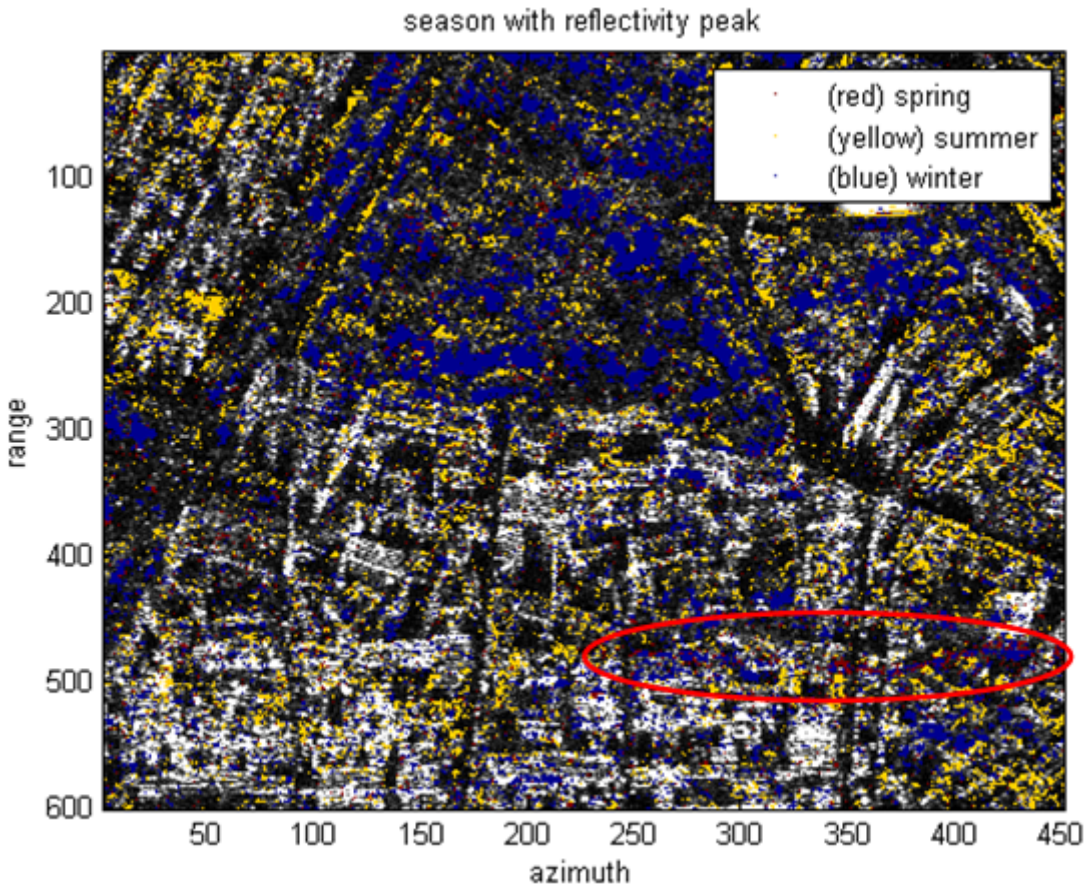

Figure 4.6: Season with reflectivity peak.

All of the points with a summer peak are not to be identified with trees or any sort of vegetation but with buildings or with the counter-phase of the tree. This matter will be further discussed in section 4.4.1.

4.2.2 Change detection-oriented

Time series analysis grounded on change detection results does not evaluate the pixel's statistics on the totality of the available time samples but distinguishes statistics before the step, the time laps when the step occurred and the statistics after the step.

The same algorithm used for standard classification has been applied to both sections, provided that the partial time series is at least 30 samples long. If this is not the case, the pixel will be labeled as not classified in order to avoid misinterpretations due to insufficient series length.

In order to highlight the importance of the length of the partial time series, a comparison of classification results based on available samples has been provided in Figure 4.7:

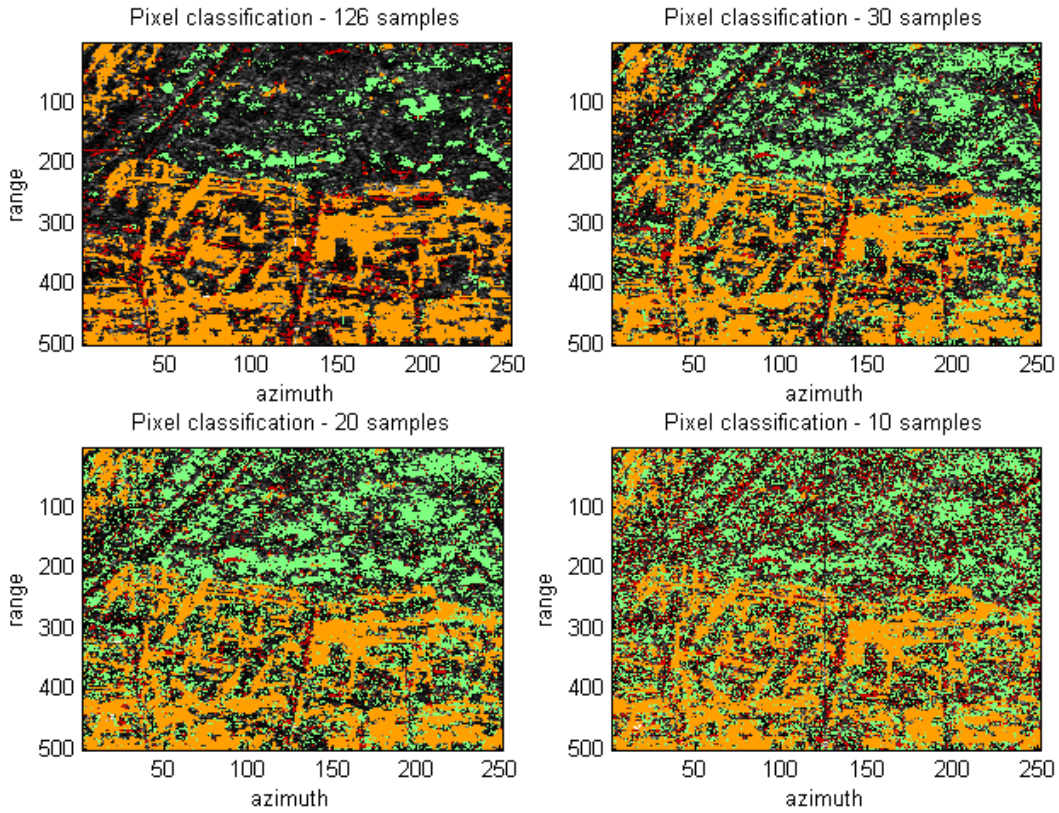

Figure 4.7: Pixel classification for various time series lengths.

As it can be seen, with 30 samples the estimation is still sufficiently accurate, especially for building classification purposes. Nevertheless, as mentioned in the specific sections of section 4.2.1, as the samples further diminish, the classification of vegetation and road pixels becomes erroneous.

A further evaluation of sample reduction has also been implemented. This second comparison (depicted in Figure 4.8) does not consider adjacent samples but sparse, sampled ones, so that remote sensing satellite conditions before TerraSAR-X could be recreated. Of course, this experiment is of academic yet not practical interest and this possibility has not been implemented in the code.

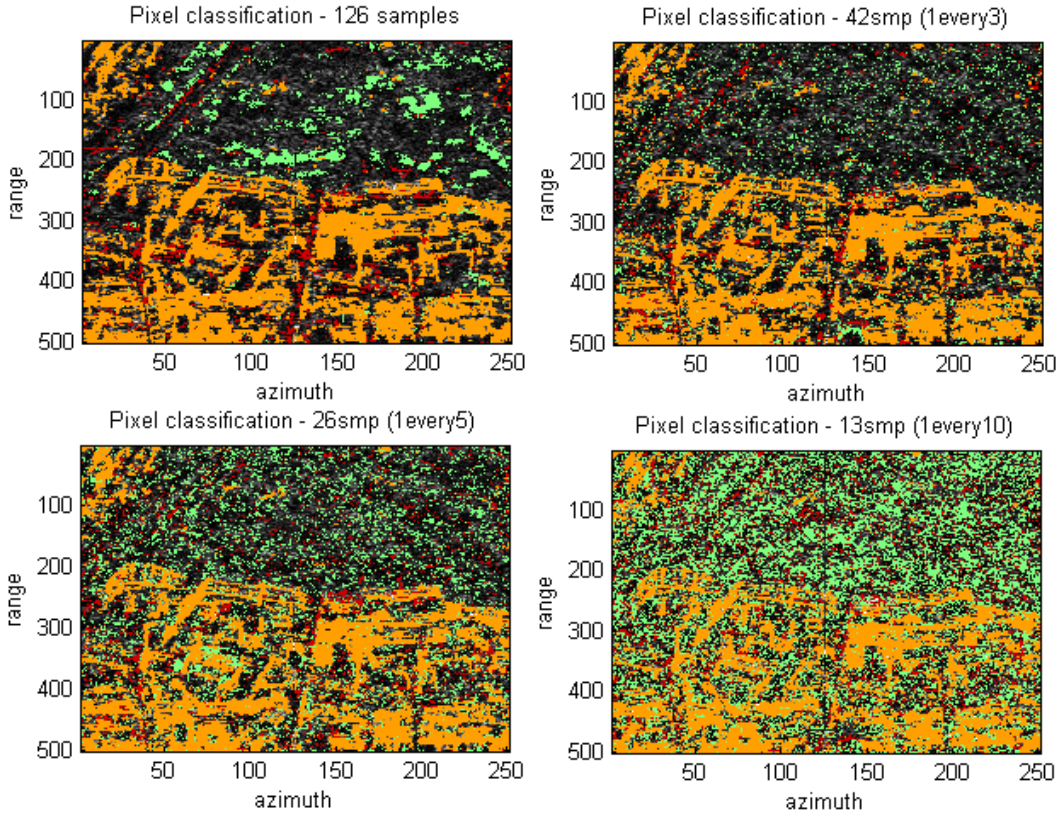

Figure 4.8: Pixel classification for various time series sampling. The case one every three (e.g. an image every 33 days) represents the results that would have been obtained by canonical remote sensing sensors before TerraSAR-X.

Predictably, a sample per month (case scenario in the top-right sub-image in Figure 4.8) is not enough for seasonal sine wave fitting.

4.3 Classification

Classification algorithms are aimed at distinguishing between classes of targets. These sets can be of a general nature (and distinguish between permanent scatterers such as buildings and incoherent distributed scatteres such as fields and forests) or identify more specific categories (buildings, trees, transportation infrastructure, etc.). These algorithms can be supervised, automatic or a combination of the two depending on whether there is a human supervision or not.

As previously mentioned, until the advent of frequent multi-temporal images, automatic algorithms worked by dividing the image into clusters (according to criteria of proximity and similarity) and subsequently assigning a class to each cluster (according to a set of parameters).

This thesis is, on the other hand, focused on pixel-by-pixel classification.

4.3.1 Interferometric coherence classification

In order to provide a first rough estimation that enables the separation of the metropolitan area from the surrounding rural area, an interferometric coherence classification has been implemented.

Since a finer classification will be performed during a later stage, the priority of this algorithm lies in velocity and not precision. Using therefore a 20×20 pixel cell resolution and images characterized by normal baseline smaller than 50m (corresponding to a time series of 51 samples), the coherence map of the whole city of Milan can be obtained and it is depicted in Figure 4.9.

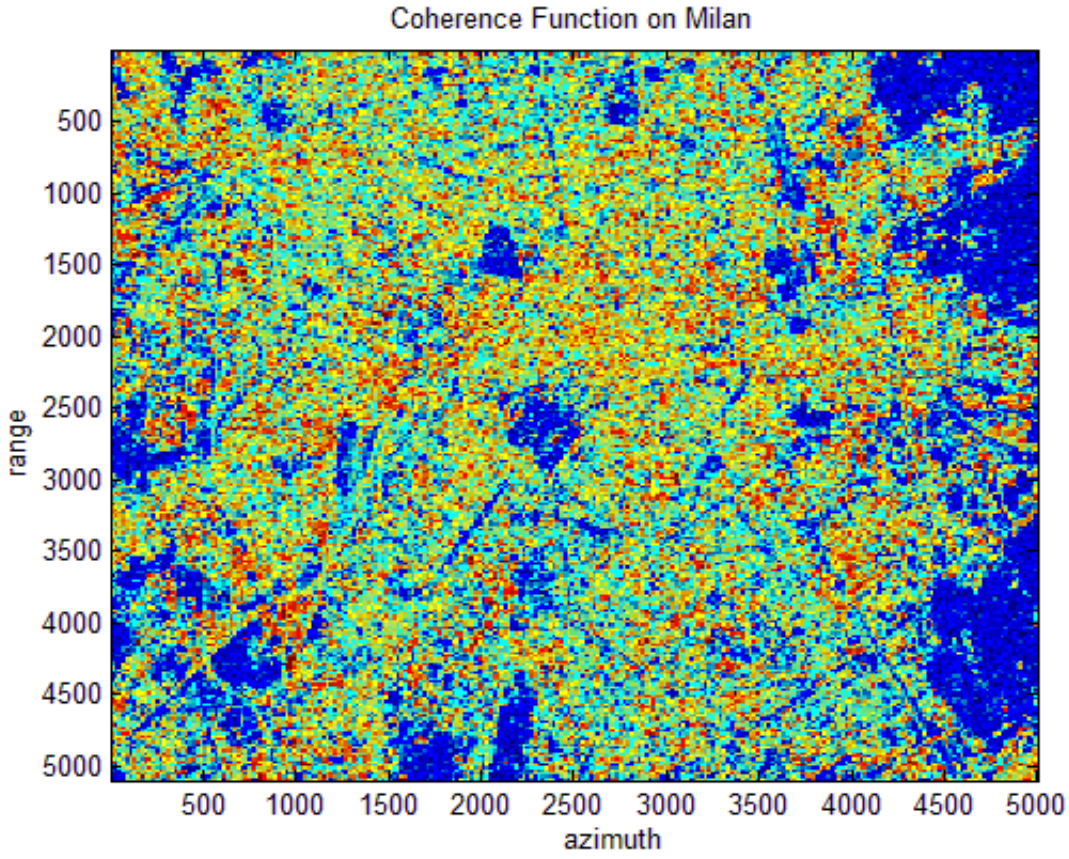

Figure 4.9: Interferometric coherence map of Milan.

Taking now all the pixel blocks with coherence higher than 0.3, a coherence mask of Milan that discerns between urban and non-urban blocks can be estimated. The value 0.3 is low; however this is the consequence of two facts:

1. 20×20 pixels correspond to a 40m $\times$ 30m ground resolution. In such a big area, both buildings and vegetation could be present, and the coherence be an average of the ensemble;

2. A false positive is not a problem due to the subsequent finer resolution.

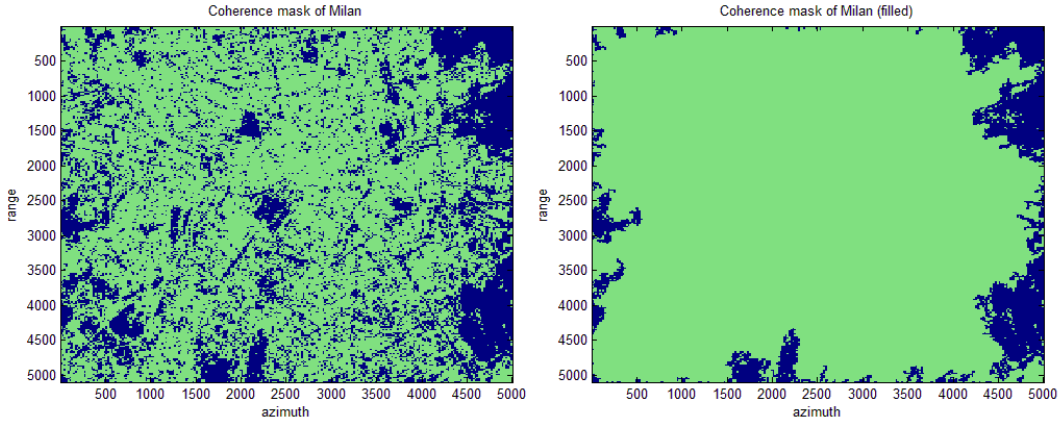

Figure 4.10: Coherence mask of Milan. On the left pixels characterized by a coherence function higher than 0.3, on the right the same mask, filled in order to separate the metropolitan area from the countryside.

As it can be noted by the results in Figure 4.10, interferometric coherence provides the means for a first rough estimation that enables the separation of the metropolitan area of interest from the surrounding countryside.

4.3.2 Standard classification

In the metropolitan area, that has been previously identified by the coherence algorithms, a finer pixel-by-pixel classification based on the amplitude's time series can be applied.

The result of this classification code on the entire city of Milan is shown in Figure 4.11:

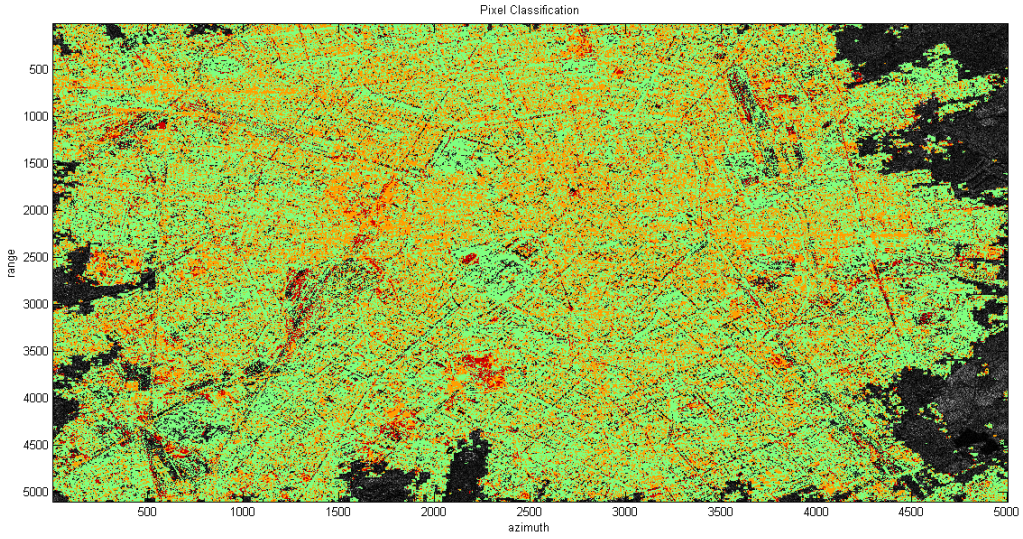

Figure 4.11: Pixel classification of the whole Milanese area. In green are vegetation pixels, in orange building pixels and in red road pixels. The preponderance of green is an optical illusion caused by the thickness of the colored dots. The results can therefore be better appreciated in zoomed sections.

The preponderance of green is an optical illusion resultant of the thickness of the colored dots drawn by the imaging algorithm. The effectiveness of the classification can be therefore better appreciated in the following Figure 4.12, which zooms into the inner area of the city delimited by the *Cerchia dei Bastioni*:

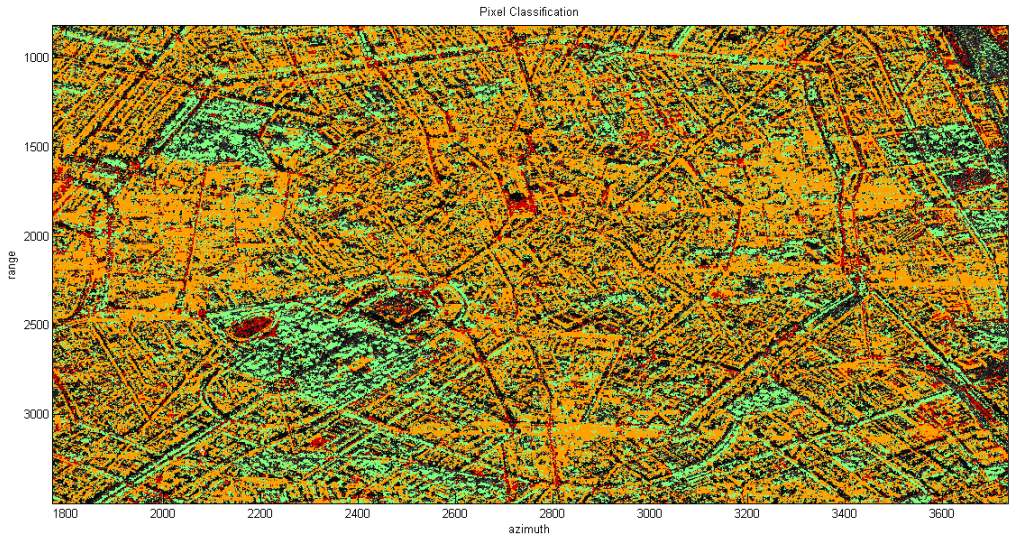

Figure 4.12: Pixel classification of the inner area of Milan delimited by the *Cerchia dei Bastioni*. In green are vegetation pixels, in orange building pixels and in red road and square pixels.

Additionally, in order to better appreciate the achievable resolution, the pixel classification for the innermost *Cerchia dei Navigli* is as depicted in Figure 4.13:

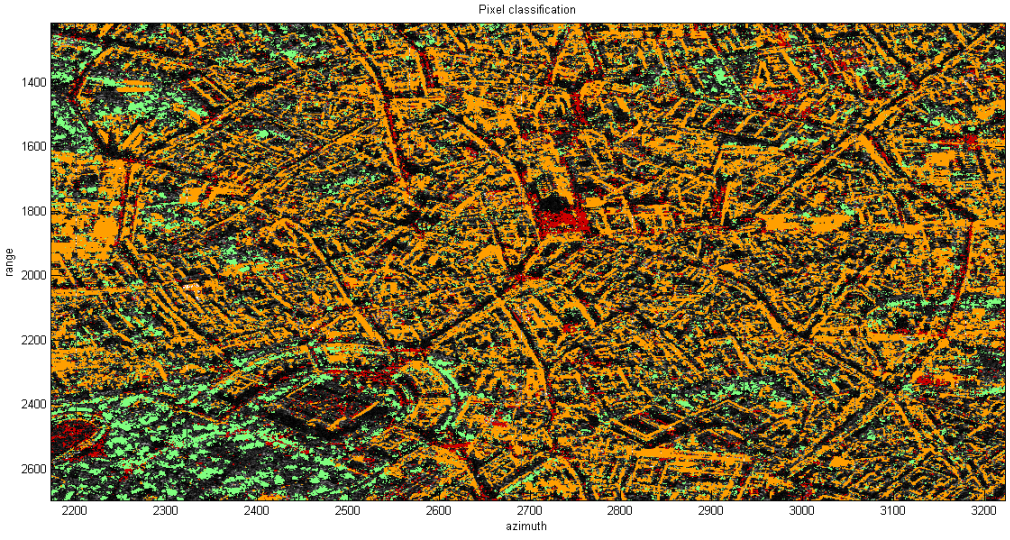

Figure 4.13: Pixel classification of the innermost area of Milan delimited by the *Cerchia dei Navigli*. In green are vegetation pixels, in orange building pixels and in red road and square pixels.

The percentage of classified pixels changes according to the area under investigation. For densely constructed areas it is around 35% whereas for parks it lowers to

15%.

These values are a consequence of two different factors:

- Shadow areas between buildings cannot be classified;
- Since the estimator only has three categories, the pixels that do not belong to either result unclassified. Typical examples are grass and bare soil.

4.3.3 Classification of pixels with a high probability step

In order to monitor urban growth it is not only important to be able to classify pixels but also to detect when changes occur, so that a new classification can be implemented, thus enabling always-current databases.

By adding step detection algorithms to the previous classification, the result in Figure 4.14 can be obtained:

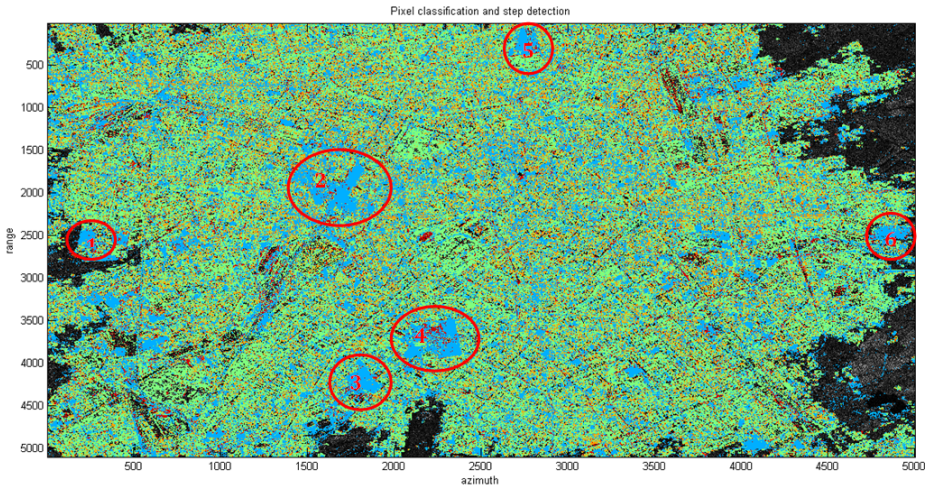

Figure 4.14: Pixel classification and step detection on the whole area of Milan. In blue are the pixels characterized by step detection.In green are vegetation pixels, in orange building pixels and in red road and square pixels.

As with the previous example, the quality is not ideal for visualizing the city in its entirety, however it still allows an immediate visualization of all the major areas that undertook requalification or modernization programmes:

1. Construction of a new wing at the *Niguarda* Hospital;
2. *Piazza Gae Aulenti* and the *Porta Nuova* Project;
3. *Parco Vittoria* residences;
4. *City Life* requalification program;
5. *Porta Vittoria* requalification program;
6. Construction of *Le Corti all'Alzaia* residences.

Zooming on *piazza Gae Aulenti* and the *Porta Nuova* area which, as mentioned in the introductory paragraph, is the area where the investigation has been focused, Figure 4.15 can be obtained. For an immediate comparison between change-detected pixels and ground-reality refer to Figure 4.18 and Figure 4.19.

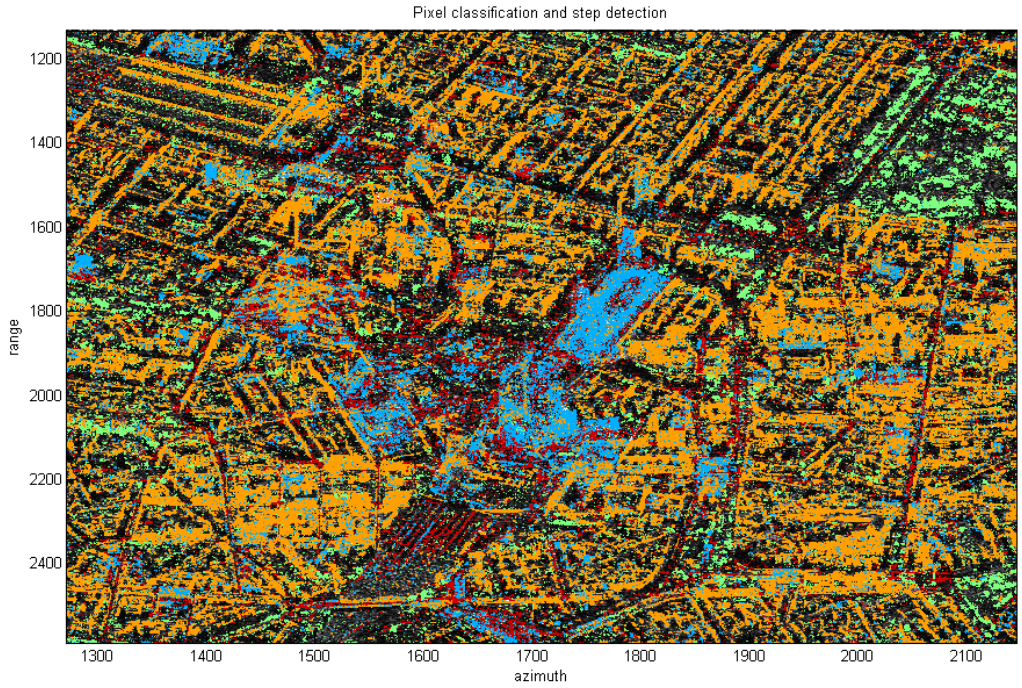

Figure 4.15: Pixel classification and step detection on *piazza Gae Aulenti* and the *Porta Nuova* area. In blue are the pixels characterized by step detection.In green are vegetation pixels, in orange building pixels and in red road and square pixels.

4.3.3.1 Classification before and after the step

Once a step is detected, it is of primary importance with respect to urban sprawl monitoring to classify what the pixel was before the step and what it became afterwards.

Applying this methodology on *piazza Gae Aulenti* and considering only the most common pixel variations so that the image is of immediate interpretation, the result in Figure 4.16 can be obtained:

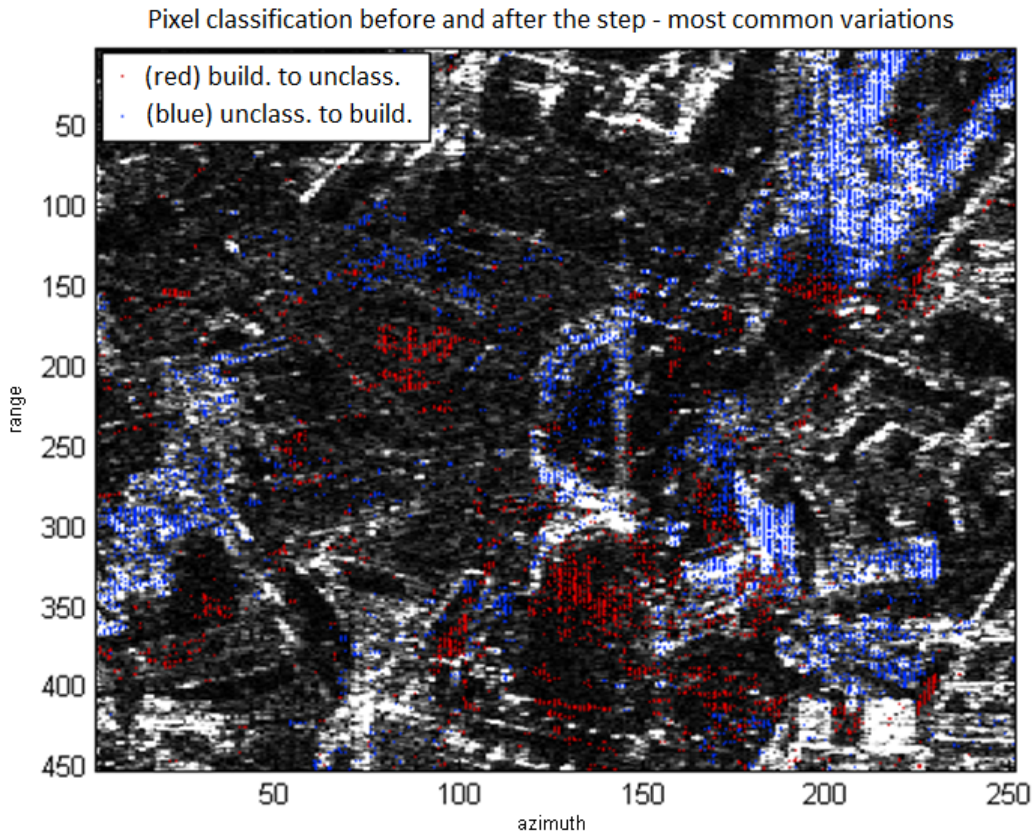

Figure 4.16: Pixel classification before and after the step - most common variations.

As it can be observed, the majority of pixels have half of their time series marked as unclassified. This is due to two reasons:

- Some partial time series are not sufficiently long in order to make an estimation;
- In order to make the foundations of the buildings, the area has been leveled and covered with dry soil. This particular type of terrain, which scatters in a very similar way to fields, was not subjected to classification.

Despite the fact that these were the most common results, other less ambiguous classifications can be obtained under the condition that more samples are available (steps in the middle of the time series). The classification before and after the step for less common variations is shown in Figure 4.17.

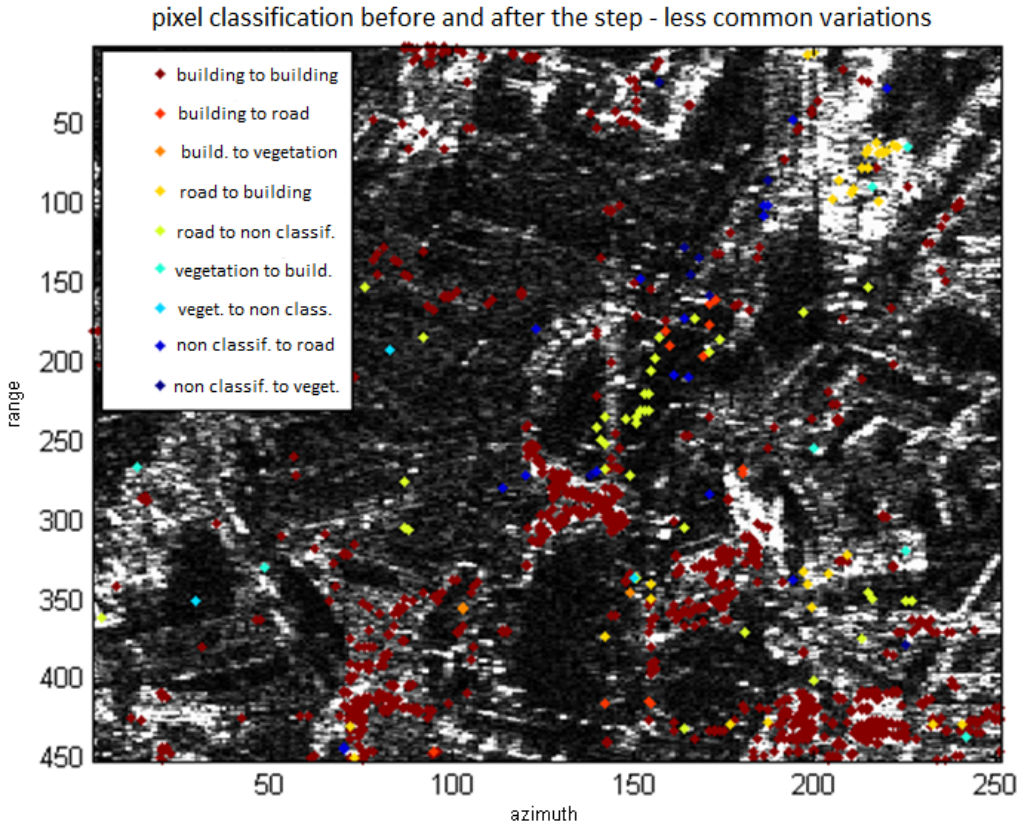

Figure 4.17: Pixel classification before and after the step - less common variations.

4.3.3.2 Growth monitoring of buildings

Another application for change detection in urban monitoring is the tracking of buildings as they grow. This is particularly important for skyscrapers as, being glass their primary covering material, they tend to have a significantly lower backscatter with respect to other buildings. This fact may lead to wrongful classification and will be further discussed in section 4.4.2.

An interesting preliminary example can be found by monitoring *piazza Gae Aulenti* and *Porta Nuova*. Taking into consideration the map and Google Earth rendering of the area (that are depicted in Figure 4.18) as means of comparison and plotting the position in time of the single steps in order to visualize the time table by which the buildings have been constructed, Figure 4.19 can be obtained.

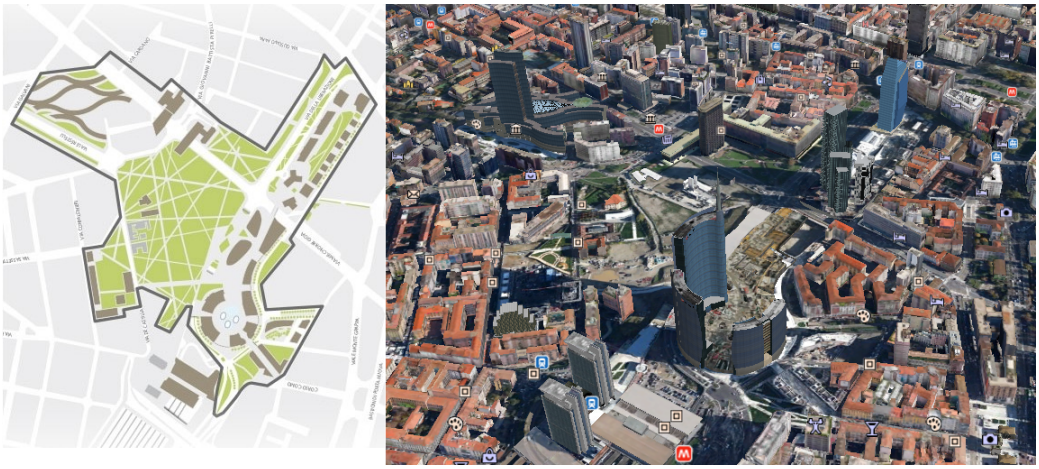

Figure 4.18: Map and Google Earth rendering of the area under analysis.

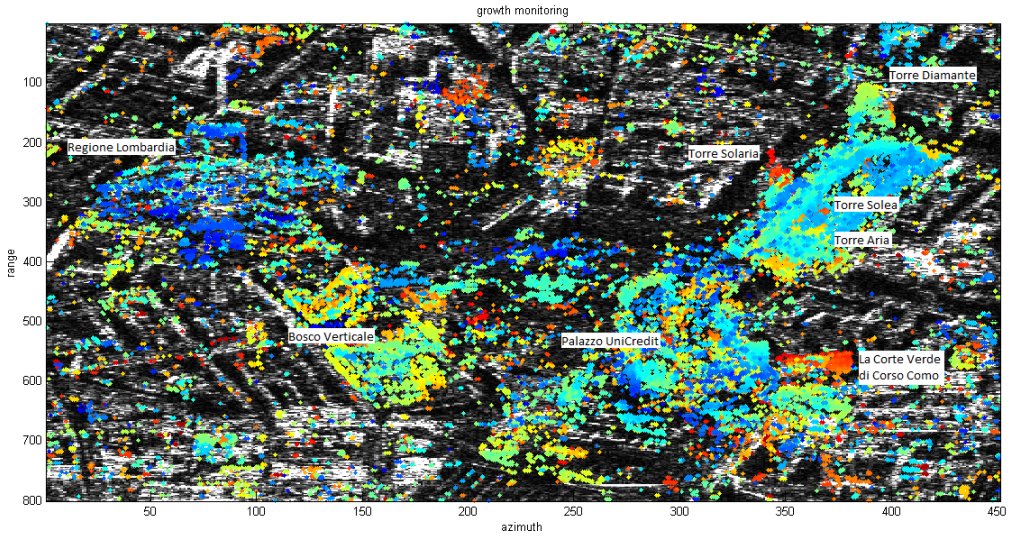

Figure 4.19: The position in time of the single steps makes it possible to monitor the growth of the skyscrapers.

As it can be seen in Figure 4.19, the newly constructed buildings are clearly identified by the change-detection algorithm which, additionally, keeps track of the time when that change occurred (blue marks the oldest and red the newest).

Taking into consideration Figure 4.19 and going from left to right and from top to bottom, interesting examples are:

- *Palazzo Regione Lombardia*: constructed between 2007 and 2010, was the first new building in the area. In the picture is correctly marked by a blue color;
- *Bosco Verticale*: constructed between 2009 and 2014, it encountered various problems since the company that was first contracted to build it went bankrupt. These delays are depicted in Figure 4.19 by a non uniform ensemble of different time positions;

- *Palazzo UniCredit*: constructed between 2009 and 2011, it is marked by a light blue color;
- *Torre Solaria, Torre Solea, Torre Aria*: constructed between 2010 and 2013. Their foundations are characterized by a light blue color whereas the top of the skyscraper assumes warmer colors. Particularly evident is the red-colored roof of *Torre Solaria*;
- *Torre Diamante*: constructed between 2010 and 2012, also assumes warmer colors going towards the top. Due to the fact that it was terminated a year before the other three towers in the *Varesine*, it does not show any red pixels;
- *La Corte Verde di Corso Como*: constructed between 2011 and 2013, it's the last building to have been constructed and therefore correctly characterized by a red color. As a matter of fact, these residences are not even present in the Google Earth rendering.

4.3.3.3 Identification of known events

Step detection algorithms can also be implemented in order to identify known events. Keeping the analysis linked to *piazza Gae Aulenti*, the two publicized construction occurrences can be detected:

- 15th October 2011, positioning of an antenna on the roof of *Palazzo UniCredit* (depicted in Figure 4.20 on the left-hand side);
- 3rd of May 2013, positioning of a cycle-pedestrian metal gangway on *via Melchiorre Gioia* (depicted in Figure 4.20 on the right-hand side).

Figure 4.20: Positioning of the antenna on the *Palazzo UniCredit* (on the left) and cycle-pedestrian on *via Melchiorre Gioia* (on the right).

Looking for steps in the before-written dates, the following Figure 4.21 can be obtained:

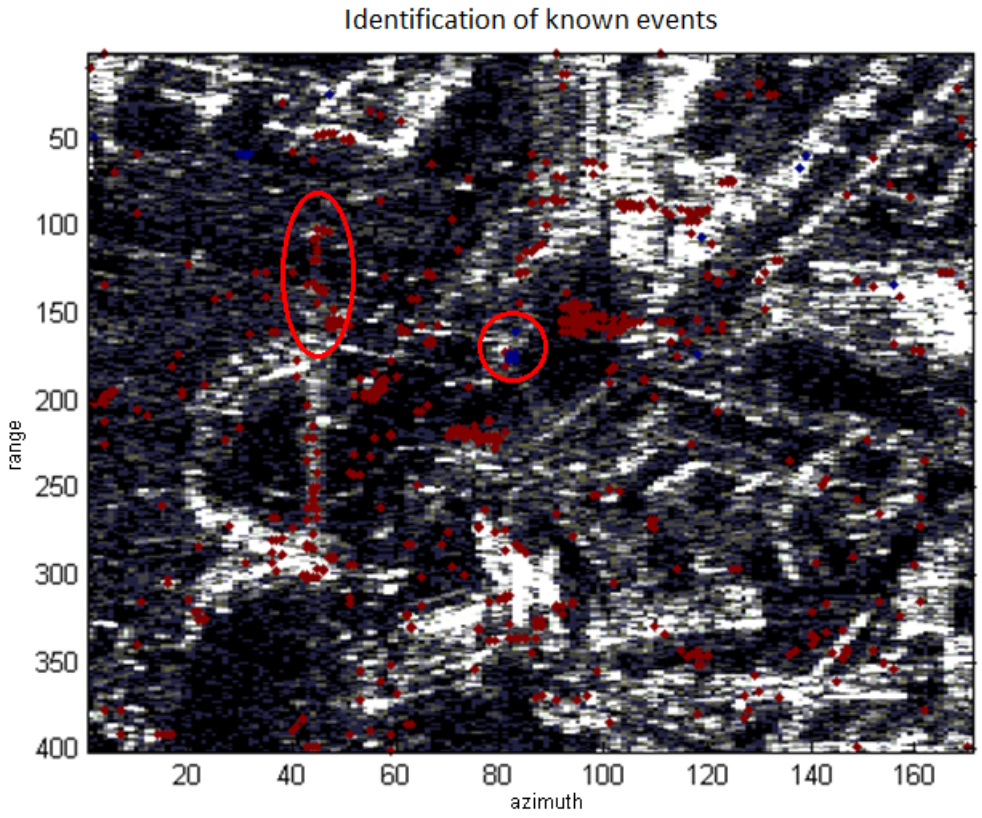

Figure 4.21: Identification of known events. In red the events corresponding to the 15/10/2011 and in blue the events corresponding to the 03/05/2013.

As it can be noted, both the events have been found although only a tiny part of the cycle-pedestrian gangway can be seen due to unfortunate geometry.

4.4 Issues and case examples

During the development of this thesis two peculiarities, originated by current conditions, appeared causing errors in the classification algorithm.

The first is the fact that some buildings or sections of building scatter with a seasonal trend and the second is the fact that glass or ceramic-covered skyscrapers are completely or partially invisible to radars.

4.4.1 Buildings characterized by seasonal trend

As it can be seen by the examples in Figure 4.22, some buildings, or parts of them, scatter with a seasonal trend characterized by a summer peak and an excursion of 200%:

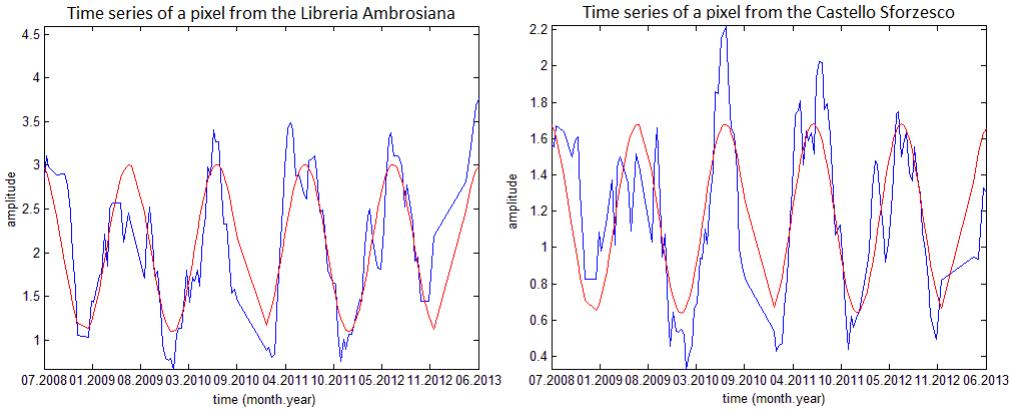

Figure 4.22: Examples of building pixels scattering with a seasonal trend.

This fact is not known: Chitar et al. in 1992 noted how urban areas were not subject to snow cover or sinusoidal fluctuations to the degree that other natural cover types were [13]. It is not however surprising that this phenomenon passed undetected throughout the years as it is only due to TerraSAR-X's revisit time that a good quality fitting of the seasonal sine wave has been possible.

A first partial mention to this problem (e.g. summer thermal dilatation and the influence of reduced temporal revisit time on interferometry under those conditions) has been discussed by Duro et al. in 2010 but as the majority of papers on the topic, this focuses on data contained in the phase and not in the amplitude.

This thesis cannot provide a conclusive answer to the reasons that cause this phenomenon, as this would require a thorough investigation which would include chemical and mechanical considerations for a great amount of materials and geometries. Nevertheless, a series of considerations and hypotheses are hereafter proposed.

4.4.1.1 Quantification of the phenomenon

This phenomenon is not easy to quantify as the majority of pixels characterized by a seasonal trend with a summer peak result unclassified.

As discussed in section 4.2.1.3, this thesis relies on the assumption that vegetation pixels are identified as such only in case of positive phase-shift of the sinusoidal seasonal trend. This fact, that is absolutely erroneous when considering crops, works in an urban environment.

Analyzing the entire data-set, 30% of pixels scattering with a sinusoidal trend and summer peak are classified as buildings. This percentage decreases when considering vegetation areas (as the *Parco Agricolo Sud Milano* and the city parks) and increases to 50% in some urban areas.

Considering a central area and a correlation between time series and seasonal trend higher than 0.8, the results in Figure 4.23 can be obtained:

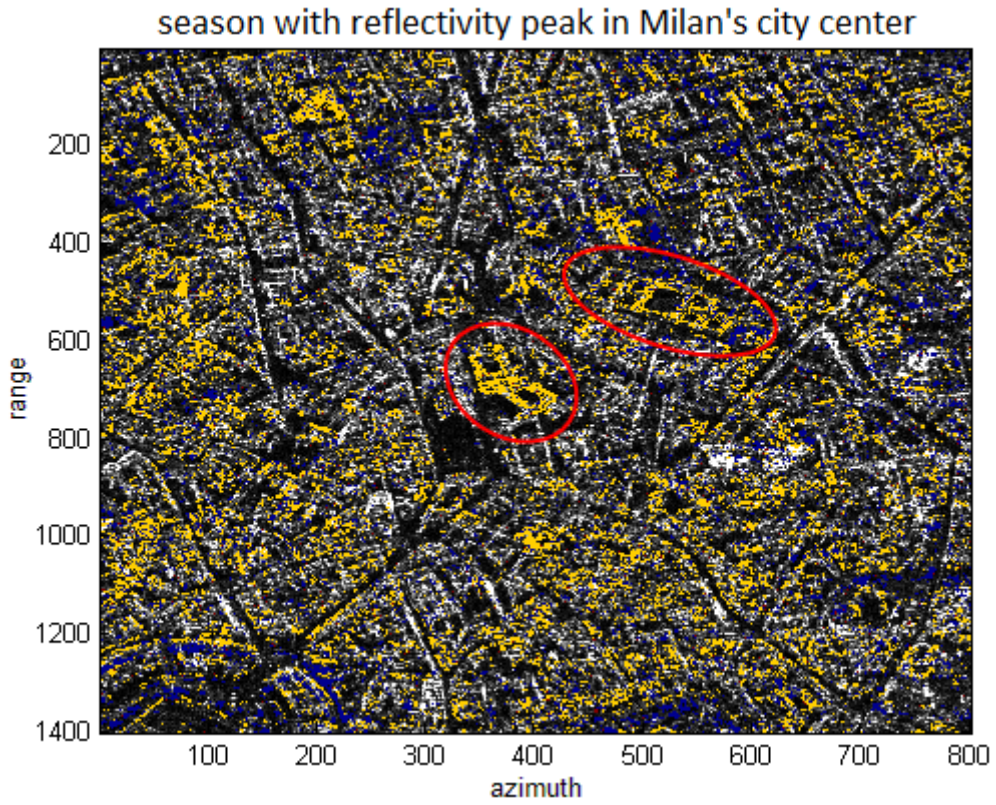

Figure 4.23: Reflective peaks in a central area of Milan. In yellow are the summer peaks whereas in blue are the winter ones. Two particularly evident examples of buildings scattering with a seasonal trend are circled in red and correspond to the *Palazzo Reale* and *Palazzo Arcivescovile* (on the left) and to the *Università statale* (on the right).

As it can be seen in Figure 4.23, in Milan's city center there are three particularly evident examples of buildings scattering with a seasonal trend. They are circled in red and correspond to the neighboring *Palazzo Reale* and *Palazzo Arcivescovile* (on the left) and to the *Univeristà statale* (on the right).

In this section the percentages are as follows:

- buildings: 38.7% of scatterers with a sinusoidal summer peak;
- vegetation: 0% of scatterers with a sinusoidal summer peak;
- roads and squares: 0.12% of scatterers with a sinusoidal summer peak;
- unclassified: 61.2% of scatterers with a sinusoidal summer peak.

Also, out of all of the pixels classified as building, 5% scatters in a seasonal summer-peaked fashion.

Vegetation pixels are an absolute 0% as a consequence that positive phase-shift has been imposed but under no circumstance it should be believed that the unclassified

pixels all correspond to vegetation pixels and for this same reason the building's percentage might also probably a bit higher.

In order to prove this, a second estimation without the positive phase-shift limitation has been implemented. Under these conditions vegetation pixels resulted being the 54% and the unclassified 7%, leading though to the erroneous classification in Figure 4.24:

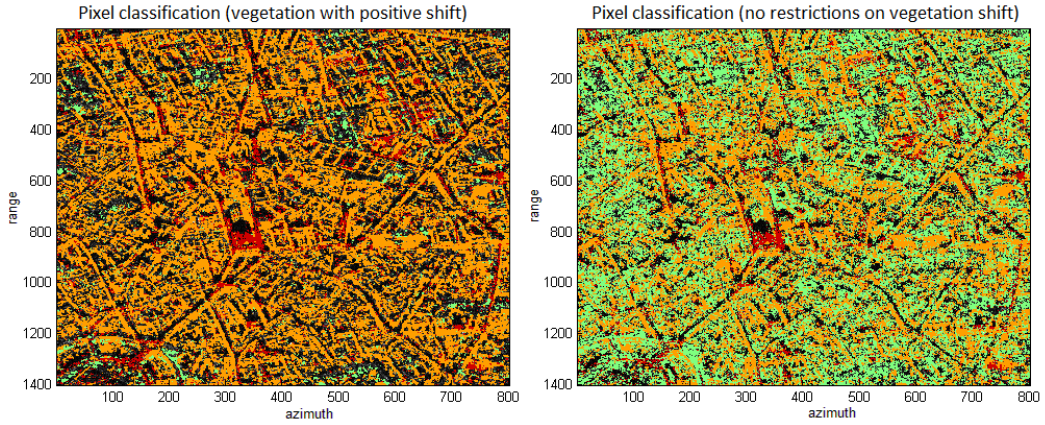

Figure 4.24: Comparison between classification results imposing vegetation pixels to have a positive phase-shift of the sinusoidal trend and with no restrictions. As predicted the second condition results erroneous .

As it appears immediately clear, it is not possible for the center-most area of Milan to have a preponderance of vegetation with respect to buildings.

4.4.1.2 Identification of the scattering position

Once determined that a certain percentage of buildings returns such an amplitude trend, an estimation of the position of the scatterers has been implemented.

In order to put this into practice, the interferometric height of permanent scatteres with respect to Milan's Digital Elevation Model has been considered.

Taking now all of the permanent scatterers that have a sinusoidal component and plotting their interferometric height versus the amplitude of their seasonal sine wave, the results in the following Figure 4.25 can be obtained:

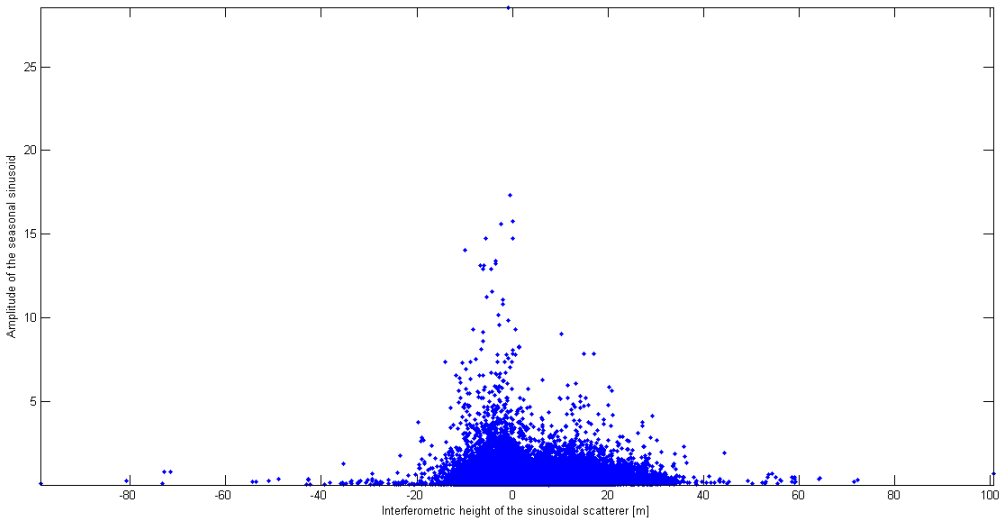

Figure 4.25: Interferometric height of the sinusoidal scatterer versus amplitude of the seasonal trend.

As it can be seen, the sinusoidal scattering origins both from the corner reflectors between pavement and building's facade and from roofs and other architectural components along its elevation. Predictably, the ground corner reflectors are the ones that enable the highest amplitudes.

4.4.1.3 First hypothesis/contribution: variation of the dielectric constant with temperature

As a first hypothesis, the variation of the dielectric constant with temperature has been considered. This chemical alteration varies according to the single material so it could not be univocally determined.

First of all, the radar cross section for dielectric constant variations has been calculated:

$$\sigma = \lim_{R\to\infty} 4\pi R^2 \frac{|E^{scat}|^2}{|E^{inc}|^2} \tag{4.1}$$

$$\sigma = 4\pi R^2 |\Gamma|^2 \tag{4.2}$$

$$\sigma = 4\pi R^2 \left| \frac{\sqrt{\varepsilon_{air}} - \sqrt{\varepsilon_{target}}}{\sqrt{\varepsilon_{air}} + \sqrt{\varepsilon_{target}}} \right|^2 = 4\pi R^2 \left| \frac{1 - \sqrt{\varepsilon_{target}}}{1 + \sqrt{\varepsilon_{target}}} \right|^2 \tag{4.3}$$

Thereafter, the amplitude's variation with the RCS has been computed:

$$a^2 = P_r = \frac{P_t G_t G_r}{(4\pi)^3 R^4} \times \lambda^2 \times \sigma = \frac{P_t G_t G_r}{(4\pi)^3 R^4} \times \lambda^2 \times 4\pi R^2 \left| \frac{1 - \sqrt{\varepsilon_{target}}}{1 + \sqrt{\varepsilon_{target}}} \right|^2 \tag{4.4}$$

$$a^2 = \frac{P_t G_t G_r}{\left(\frac{4\pi}{\lambda}\right)^2 R^2} \times \left| \frac{1 - \sqrt{\varepsilon_{target}}}{1 + \sqrt{\varepsilon_{target}}} \right|^2 \tag{4.5}$$

$$a = |a_0| \times \left| \frac{1 - \sqrt{\varepsilon_{target}}}{1 + \sqrt{\varepsilon_{target}}} \right| \tag{4.6}$$

Where a_0 is the generic amplitude of any target at a certain distance from the radar.

In the case of asphalt, its dielectric variations with temperature have been found in a paper from the *Council for Scientific and Industrial Research* of South Africa [14]. They are shown in Figure 4.26.

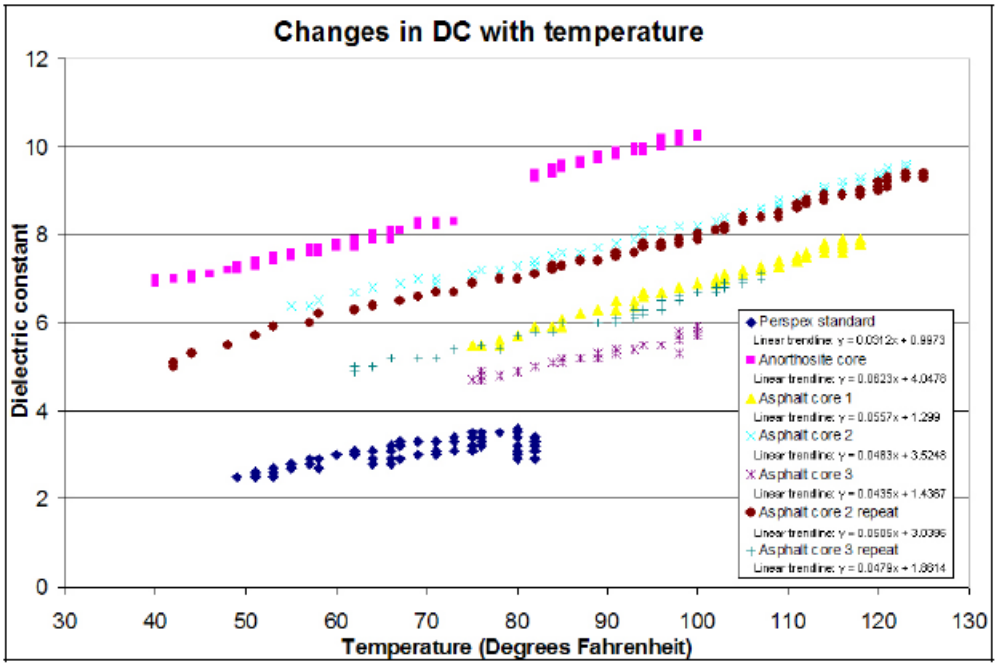

Figure 4.26: Asphalt's dielectric constant variations with temperature. Source: *Council for Scientific and Industrial Research* of South Africa.

Utilizing these values, the amplitude changes result in:

- $\varepsilon_{asphalt,5^\circ} = 5$ and therefore $a_{asphalt,5^\circ} = |a_0| \times 0.382$;
- $\varepsilon_{asphalt,21^\circ} = 6.5$ and therefore $a_{asphalt,21^\circ} = |a_0| \times 0.436$;
- $\varepsilon_{asphalt,38^\circ} = 8$ and therefore $a_{asphalt,38^\circ} = |a_0| \times 0.477$.

Corresponding to an increase of 25% in the received amplitude when passing from 5 °C to 38 °C. Considering that in Milan the temperature easily drops under 5 °C, it's likely that the actual percentage is higher. Unfortunately, data for less than 40 °F (equal to 5 °C) was not available.

As mentioned, though, this percentage varies according to the single material, so it's not of a general validity and percentages in other cases could be a lot higher or close to zero. Unfortunately, not many studies have been found on the variation of dielectric constant with temperature; none with other construction materials that

could have been of interest towards this inquiry.

Nevertheless this result shows how some chemical variations might occur as the temperature rises and account for a part of the amplitude's fluctuations.

4.4.1.4 Second hypothesis/contribution: variations in surface roughness

Another hypothesis that has been considered is the variation of surface roughness with temperature: frequently during summer the pavements tend to partially melt, becoming therefore smoother.

Before even beginning with this calculation, the estimation of the Rayleigh and Frauenhofer criterions for rough surfaces has been implemented. Thanks to these tools, the minimum height after which the coarseness can be neglected can be determined.

According to the Rayleigh criterion:

$$h_r \leq \frac{\lambda}{8\cos(\theta_{inc})} \tag{4.7}$$

That, with the Milan's TerraSAR-X settings corresponds to:

$$h_r \leq \frac{3.1}{8\cos(37°)} = 0.49\text{cm} \tag{4.8}$$

And, according to the more stringent Frauenhofer criterion:

$$h_f \leq \frac{\lambda}{32\cos(\theta_{inc})} \tag{4.9}$$

Leads to:

$$h_f \leq \frac{3.1}{32\cos(37°)} = 0.12\text{cm} \tag{4.10}$$

Since variations of tenths of millimeters are plausible, the Dubois empirical model for rough surface scattering has been calculated.
According to this model, the normalized radar cross section for HH polarization is as follows:

$$\sigma^0_{HH} = 10^{-2.75}\frac{\cos(\theta)^{1.5}}{\sin(\theta)^5}10^{0.028\varepsilon\tan(\theta_{inc})}\left(ks\sin(\theta_{inc})\right)^{1.4}\lambda^{0.7} \tag{4.11}$$

where s is a statistical roughness parameter defined as the root mean square height of the surface and is measured in centimeters and k is the wavenumber.

Substituting the theoretical parameters with those of our system, the linear trend depicted in Figure 4.27 can be obtained.

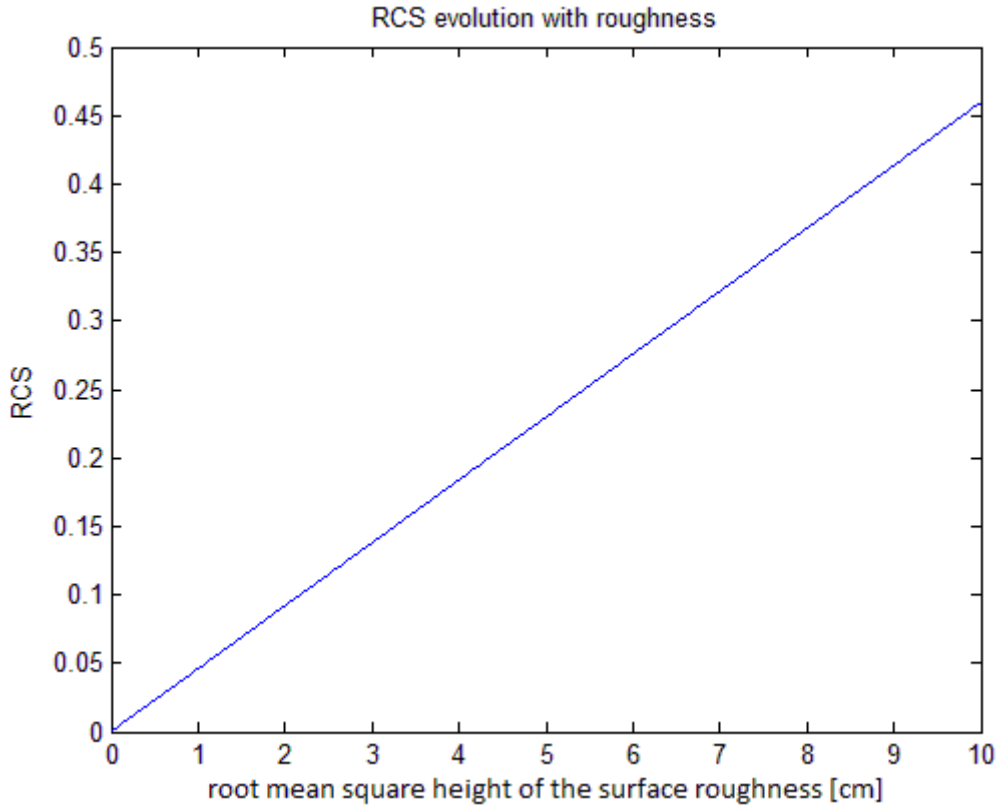

Figure 4.27: RCS Evolution with roughness Accirding to the Dubois model.

Considering now the case of perfectly smooth pavement that allows full reflection on the building's facade and subsequent full reflection towards the radar, the received amplitude is:

$$a_{smooth} = a_0 \times (1 - RCS) = a_0 \tag{4.12}$$

When the pavement is rough, though, not all of the energy is scattered towards the building and some is lost. Considering a 2cm maximum roughness:

$$a_{rough} = a_0 \times (1 - RCS) = a_0 \times 0.9 \tag{4.13}$$

Therefore from a completely rough to a completely smooth pavement and increment of 11.11 % in the received amplitude can be detected.

4.4.1.5 Third hypothesis/contribution: thermal dilatation

Thermal dilatation of buildings is a known, documented fact that has been monitored with interferometry by numerous authors. Elevation-speaking it is in the order of tenths of millimeters [15] but what is unclear is the effect that such dilatations may introduce in the response of the amplitude.

A hypothesis that could not be numerically confirmed is the possibility that some buildings may expand in a convex fashion, making therefore the corner reflectors

between the pavement and the facade become acute. This geometric modification would thus increase the backscattering towards the radar.

4.4.2 Stealth buildings

Another problem for the algorithm is the fact that nowadays more and more buildings are glass-covered skyscrapers and therefore cannot be properly seen by the radar.
Some exemplifying cases are presented in the following sections.

4.4.2.1 The *Pirelli* skyscraper

Completed in 1958 under request of Alberto Pirelli, the president of the Pirelli Company, with its 127 meters it has been Italy's tallest building for almost forty years.
As designed by the architect Gio Ponti, (and depicted in the front elevation depicted in Figure 4.28 on the right-hand side) the high-rise edifice is completely covered by glass, ceramic and terracotta mosaic tiles and litho-ceramic components. On the roof there is a metallic structure.

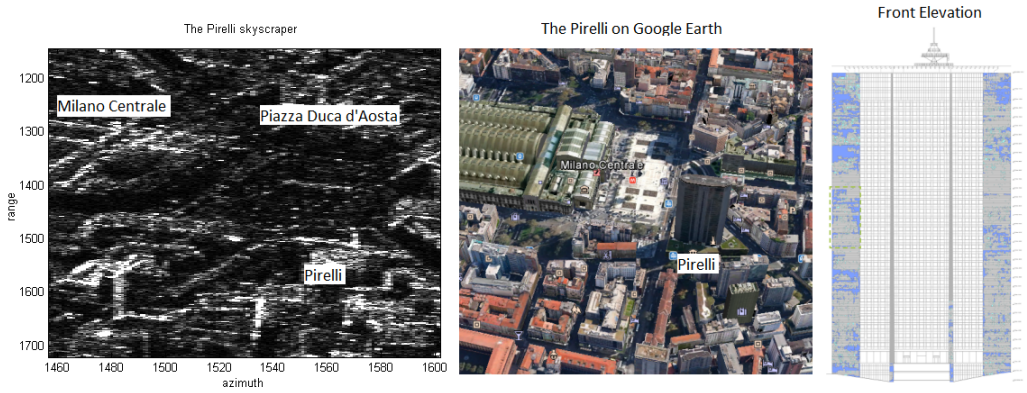

Figure 4.28: The Pirelli skyscraper. On the left its SAR image, in the center its Google Earth rendering and on the right its front elevation.

As a consequence of construction materials, it can be seen in the left-hand side of Figure 4.28 that the *Grattacielo Pirelli* is almost invisible to the radar with the exception of its roof.

4.4.2.2 The *Torre Diamante*

The *Torre Diamante* is one of the skyscrapers in the business district within the *Porta Nuova* area. It has been constructed between 2010 and 2012 and its growth has therefore been monitored by the available data-set.
Its curtain wall facade with floor to floor ceiling glass enables all of the load-bearing metal components to be hidden to the radar. Brise-soleil components for protection against direct sun light are visible to the radar on the eastern side of the building.

This combination of factors leads to the SAR image on the left-hand side of Figure 4.29:

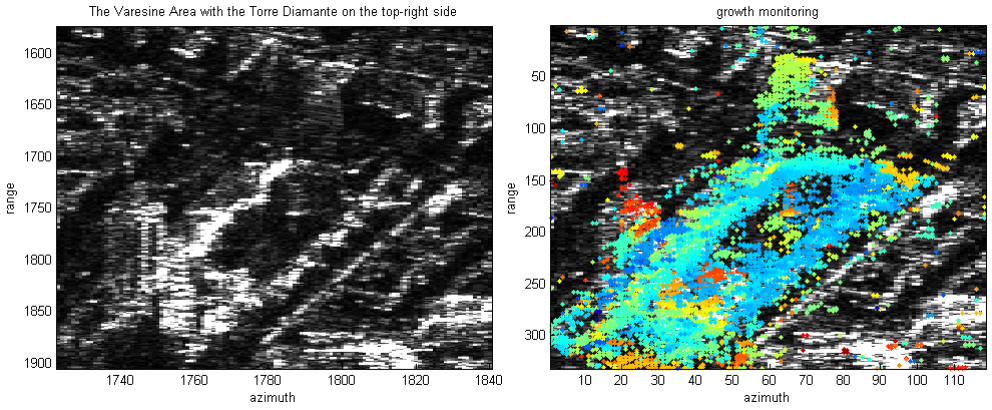

Figure 4.29: Detection of the *Torre Diamante*. On the left the SAR image and on the right the combination of the SAR image with step detection aimed at growth monitoring. As it can be seen only the right-hand side of the building (corresponding to the eastern side) is partially visible thanks to the brise-soleil elements.

As it can be seen, only the right-hand side of the building (corresponding to the eastern side) is partially visible thanks to the brise-soleil elements that act like corner reflectors. The presence and orientation of these components can be better comprehended with the *Torre Diamante*'s height elevation depicted in Figure 4.30.

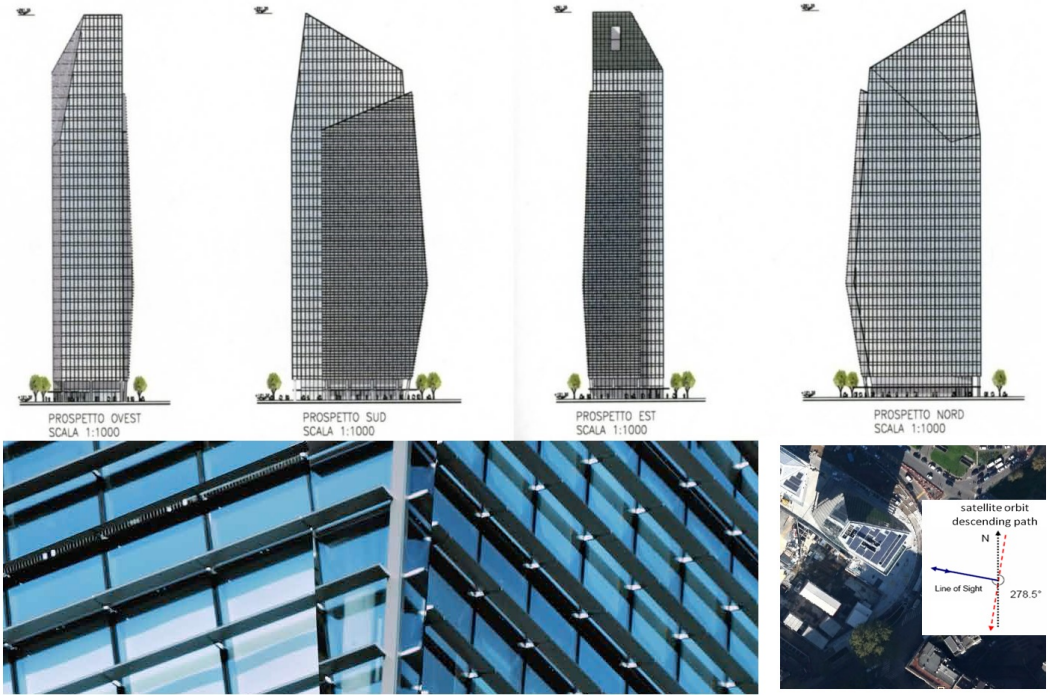

Figure 4.30: Height elevation of the *Torre Diamante* (top). Zoom on the brise-soleil elements (bottom left) and line-of-sight geometry explanation (bottom right). The radar sees the north side of the building (which is completely stealth and is on the left side in the SAR image) and the east side of the building (which is partially visible thanks to the brise-soleil elements and is on the right side in the SAR image)

Despite the invisibility of the skyscraper naked-eyed, due to change detection it is still possible to detect its growth, as confirmed by the results on the right-hand side of Figure 4.29. This very strong tool should be used in classification algorithms in combination to geo-referencing in order to avoid missed classifications.

Chapter 5

Conclusions

The exploitation of the newly-available TerraSAR-X images acquired with a revisit time of 11 days, allowed the implementation of a classification algorithm characterized by three classes of targets: buildings, vegetation, roads and squares.

Such algorithm, integrated by change detection, is enabled to monitor topographic changes. Due to this reason, it has been identified as a means for integrating ISPRA's land use monitoring techniques.

More specifically, it has been shown that every pixel assumes a certain trend in time that depends on the type of scatterer it corresponds to. For three classes of targets this trend is particularly distinctive and can be therefore exerted for classification purposes.

In order to identify this characterizing trend, some mathematical tools such as mean, kurtosis and entropy need to be implemented. Furthermore, the correlation to a seasonal sinusoidal trend has been deemed of primary importance in order to identify vegetation pixels and the estimation of the interferometric coherence of the phase allowed a first rough distinction between the metropolitan area (by means of the identification of coherent stable scatteres such as buildings) and the surrounding countryside (by means of the identification of incoherent targets such as vegetation).

Buildings time series proved to be characterized by high amplitudes (at least 45% of the amplitude dynamics on a logarithmic scale) and relatively low entropy (lower than 80% of the dynamics).

Roads and squares time series proved to be characterized by low amplitudes (lower than 45% of the amplitude dynamics on a logarithmic scale), high entropy (at least 80% of the dynamics) and high kurtosis (at least 62% of the kurtosis dynamics on a logarithmic scale).

Vegetation time series proved to be characterized by low amplitudes (lower than 45% of the amplitude dynamics on a logarithmic scale), high entropy (at least 80% of the dynamics) and high correlation (at least 80%) with a seasonal sinusoidal trend that was subjected to a positive phase-shift.

During a later stage, the classification algorithm was integrated with change detection. Thanks to this further analysis, it became feasible to classify the targets before and after the change occurred (provided that a sufficient amount of samples is available), monitor the growth of new buildings and identify known events (by exploiting the knowledge in the time position of the step).

Finally, two peculiarities that appeared during the development of the thesis became object of investigation. The first one is the presence of buildings that scatter with a sinusoidal trend in time. A definitive answer could not be provided for this matter that has been so far attributed to a variation of the dielectric constant of some materials with temperature, a variation in surface roughness and thermal dilatation. The second one regards the stealth nature of some skyscrapers. In this case the source is well known (e.g. glass used as covering material is highly dielectric) but a means of overcoming the consequent classification errors has been proposed.

As a result of this work, the following recommendations can be made:

- The number of classes could be increased by analyzing other pixel's time series. Examples are water basins and bare lands (such as grasslands and dry terrains);
- Further analyses could be implemented by comparing different polarizations;
- The correlation to known meteorological events could be further investigated:
    - Conclusions should be drawn on the additional information provided by the temperature correlation and be consequently exploited;
    - Data from local weather stations, evenly spaced throughout the territory, should be acquired;
    - Other meteorological data such as humidity and rain should also be investigated.
- A satellite using longer wavelengths could be considered in order to enable the detection of buildings covered by canopy;
- Interferometry could be implemented in order to calculate the height (or monitor the incremental height) of buildings;
- The images could be geocoded in order to provide the data in a geographical reference unit that could be easily implemented by ISPRA;
- Further research could be done on the scattering mechanisms and construction materials of buildings in order to provide a final conclusion on the reasons why some scatter with a sinusoidal trend;
- A code that detects the growth of a building and automatically assigns it to its class could be implemented in order to avoid erroneous classification in case of skyscrapers.

Bibliography

[1] ISPRA. Il consumo di suolo in Italia. 2014.

[2] Alessandro Ferretti. Satellite InSAR Data, Reservoir Monitoring fro Space. EAGE. Milano, November 2013.

[3] A. Monti Guarnieri, RADAR Systems and Localization, III edition, Politecnico di Milano, January 2011.

[4] A. Monti Guarnieri, RADAR Systems and Localization, III edition, Politecnico di Milano, January 2011.

[5] Seasat Satellite's Synthetic Aperture Radar: History & Tech-Specs [online]. Alaska Satellite Facility. Available from: https://www.asf.alaska.edu/seasat/about/

[6] Principles & Applications of Imaging Radar. Edited by Floyd M. Henderson and Anthony J. Lewis. Radar Applications in Urban Analysis, Settlement Detection and Population Estimation. John Wiley & Sons, 1998.

[7] E. Knott, J. F. Schaeffer, M. T. Tuley, Radar Cross Section, Second Edition. SciTech Publishing Inc. 15 July 2004.

[8] ESA Radar Courses. Available from: http://earth.esa.int/applications/data_util/SARDOCS/spaceborne/Radar_Courses/.

[9] Ramon F. Hanssen. Radar Interferometry. Data interpretation and Error Analysis. Netherlands: Kluwer Academic Publishers, 2001.

[10] Lawrence T. DeCarlo. On the Meaning and Use of Kurtosis. Fordham University, 1997.

[11] Giuseppe Drufuca, Problemi Inversi, C.U.S.L Milano, 2004.

[12] Roberta Quero, Analisi Statistica di dati SAR di ampiezza per applicazioni di change detection e classificazione, Politecnico di Milano, Anno Accademico 2009/2010.

[13] Principles & Applications of Imaging Radar. Edited by Floyd M. Henderson and Anthony J. Lewis. Radar Applications in Urban Analysis, Settlement Detection and Population Estimation. John Wiley & Sons, 1998.

[14] A. Maharaj, R. Leyland. The dielectric constant as a means of assessing the properties of road construction materials. Pretoria, August 2010.

[15] O. Monserrat et al., The Thermal Expansion Component of Persistent Scatterer Interferometry Observations, September 2011